Spatiotemporal Characteristics of the Near-Surface Turbulent Cascade at the Submesoscale in the Drake Passage

P. F. TEDESCO,[a] L. E. BAKER,[b] A. C. NAVEIRA GARABATO,[c] M. R. MAZLOFF,[d] S. T. GILLE,[d]
C. P. CAULFIELD,[e] AND A. MASHAYEK[a]

[a] Department of Earth Sciences, University of Cambridge, Cambridge, United Kingdom
[b] School of Mathematics, University of Edinburgh, Edinburgh, United Kingdom
[c] Ocean and Earth Science, University of Southampton, Southampton, United Kingdom
[d] Scripps Institution of Oceanography, University of California, San Diego, La Jolla, California
[e] Department of Applied Mathematics and Theoretical Physics, University of Cambridge, Cambridge, United Kingdom

(Manuscript received 14 June 2023, in final form 24 October 2023, accepted 2 November 2023)

ABSTRACT: Submesoscale currents and internal gravity waves achieve an intense turbulent cascade near the ocean surface [depth of 0–$O(100)$ m], which is thought to give rise to significant energy sources and sinks for mesoscale eddies. Here, we characterize the contributions of nonwave currents (NWCs; including eddies and fronts) and internal gravity waves (IGWs; including near-inertial motions, lee waves, and the internal wave continuum) to near-surface submesoscale turbulence in the Drake Passage. Using a numerical simulation, we combine Lagrangian filtering and a Helmholtz decomposition to identify NWCs and IGWs and to characterize their dynamics (rotational versus divergent). We show that NWCs and IGWs contribute in different proportions to the inverse and forward turbulent kinetic energy cascades, based on their dynamics and spatiotemporal scales. Purely rotational NWCs cause most of the inverse cascade, while coupled rotational–divergent components of NWCs and coupled NWC–IGWs cause the forward cascade. The cascade changes direction at a spatial scale at which motions become increasingly divergent. However, the forward cascade is ultimately limited by the motions' spatiotemporal scales. The bulk of the forward cascade (80%–95%) is caused by NWCs and IGWs of small spatiotemporal scales ($L < 10$ km; $T < 6$ h), which are primarily rotational: submesoscale eddies, fronts, and the internal wave continuum. These motions also cause a significant part of the inverse cascade (30%). Our results highlight the requirement for high spatiotemporal resolutions to diagnose the properties and large-scale impacts of near-surface submesoscale turbulence accurately, with significant implications for ocean energy cycle study strategies.

KEYWORDS: Southern Ocean; Eddies; Fronts; Internal waves; Turbulence; Ocean models

1. Introduction

Ocean circulation involves interactions between motions over a wide range of spatiotemporal scales, from the global-scale overturning circulation to microscale turbulence. Energy budgets—accounting for energy sources, sinks, and transfers—offer an insightful way to unravel the ocean circulation, allowing quantification of the main oceanic drivers and processes, based on energy conservation (Ferrari and Wunsch 2009, 2010).

The kinetic energy (KE) injected by atmospheric forcing at the large scale is transferred across scales down to the microscale, and ultimately to the dissipative scale, by a turbulent KE cascade (Ferrari and Wunsch 2009, 2010; Müller et al. 2005). Much progress has been made in describing KE pathways from basin scales ($L \sim 10^3$ km; months–years) to the mesoscale ($L \sim 10$–100 km; T about weeks–months). However, questions remain on the KE pathways between the mesoscale and intermediate range of the submesoscale ($L \sim 0.1$–10 km; $T \sim$ hours–day).

Mesoscale eddies are ubiquitous in the ocean and account for 80% of the total KE (Wunsch 2007; Ferrari and Wunsch 2009). In addition to being a key component of the global ocean energy budget, mesoscale eddies shape the quasi-stationary circulation and background stratification by substantially transporting (horizontally and vertically) momentum, buoyancy, dissolved gases, and biogeochemical tracers (Hallberg and Gnanadesikan 2006; Griffies et al. 2015; Sun et al. 2019). Understanding the KE pathways that sustain the mesoscale eddy reservoir (i.e., KE sources and sinks associated with interactions with other motions) is therefore essential for understanding regional and global ocean dynamics.

At the spatiotemporal scales of mesoscale eddies, motions are dominated by near-geostrophic and hydrostatic balances, which correspond to a Rossby number $\mathrm{Ro} \ll 1$—with Ro the ratio of Coriolis time scale to the flow time scale, and provides a measure of the extent of geostrophic balance of the flow—and a Richardson number $\mathrm{Ri} \gg 1$—with Ri quantifying the flow stability to vertical shear instabilities (Charney 1971; Gill 1982) (Ro in the Drake Passage is shown in Fig. 1). In this quasigeostrophic regime, an inverse turbulent cascade transfers KE upscale toward larger horizontal and vertical scales (Rhines 1977, 1979; Salmon 1980). The dissipation of mesoscale eddy KE—necessary for achieving a stationary ocean circulation—occurs in surface and bottom boundary layers, upon which wind and bottom stresses act (Salmon 1980; Hughes and Wilson 2008).

Denotes content that is immediately available upon publication as open access.

Corresponding author: Pauline Tedesco, pfmt2@cam.ac.uk

DOI: 10.1175/JPO-D-23-0108.1

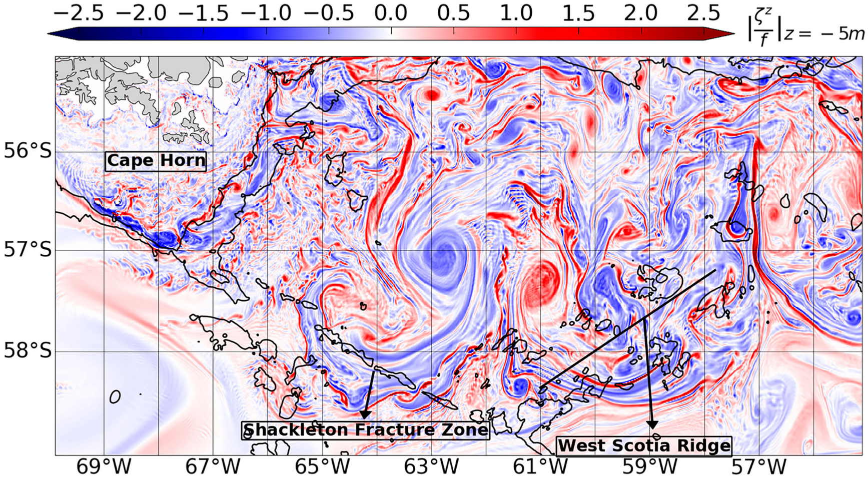

FIG. 1. Near-surface motions in the Drake Passage at wintertime. Snapshot of near-surface vertical component of normalized relative vorticity ($|\zeta^z/f|$), as modeled by a $dx \sim 1$ km numerical simulation based on the MITgcm model. Black contours show the 1000- and 3000-m isobaths, and major topographic features are labeled. The straight black line denotes the extension of the West Scotia Ridge.

In recent years, submesoscale turbulence near the ocean surface [depth of 0–$O(100)$ m] has been increasingly documented to cause an inverse and/or a forward turbulent cascade, which respectively energizes or reduces the KE reservoir of mesoscale eddies (Qiu et al. 2014; Sasaki et al. 2014; Uchida et al. 2017; Schubert et al. 2020; Dong et al. 2020; Naveira Garabato et al. 2022; Srinivasan et al. 2023). Near-surface submesoscale turbulence, therefore, plays a pivotal role in the ocean energy budget by driving dual (inverse and forward) turbulent cascades. In addition, submesoscale turbulence modulates the near-surface stratification (Klein et al. 2019; Gula et al. 2022; Taylor and Thompson 2022) by transferring tracer variance downscale, analogous to the forward energy turbulent cascade. It also shapes the characteristics of submesoscale currents, which then redistribute (horizontally and vertically) momentum, buoyancy, nutrients, and gases. The heterogeneities generated at the ocean surface subsequently modulate air–sea flux.

The near-surface ocean [depth of 0–$O(100)$ m] hosts the most energy-dense turbulence encompassing the surface boundary layer and the mixed layer (Fox-Kemper et al. 2022). It is populated by oceanic motions in the submesoscale range of distinct scales and dynamics, which can extend below the mixed layer. These motions include surface-intensified submesoscale currents (Naveira Garabato et al. 2022; Capó and McWilliams 2022) and the surface expression of internal gravity waves (Savage et al. 2017; Torres et al. 2018; Lahaye et al. 2019; Baker and Mashayek 2021). A key issue yet to be resolved is how this "zoo" of motions contributes to the near-surface turbulent KE cascade at the submesoscale and, in turn, how it shapes the mesoscale eddy KE reservoir.

Submesoscale currents include submesoscale eddies and anisotropic elongated fronts and filaments (Fig. 1). They span an intermediate dynamical range between near-geostrophically-balanced mesoscale eddies [Ro $\ll$ 1; spatial scales of O(10–100) km] and nearly isotropic boundary layer turbulence (Ro $\gg$ 1; spatial scales <0.1 km) (McWilliams 2016; Taylor and Thompson 2022). The submesoscale range is characterized by the increased importance of ageostrophic effects, and has partially geostrophically balanced dynamics (Ro $\sim$ 1 in Fig. 1, and Ri $\sim$ 1). The contribution of submesoscale currents to the inverse and forward turbulent KE cascades is thought to be driven by their partitioning into geostrophic and ageostrophic components (Capet et al. 2008a,b; Molemaker et al. 2010; Callies and Ferrari 2013; Srinivasan et al. 2023).

The near-surface ocean is also populated by near-inertial motions and by the surface expression of internal gravity waves, including near-inertial waves, internal tides, and lee waves (Savage et al. 2017; Torres et al. 2018; Lahaye et al. 2019; De Marez et al. 2020; Baker and Mashayek 2021, 2022). These have horizontal scales O(1–100) km—overlapping with the scale of mesoscale eddies and submesoscale currents—and high frequencies in the reference frame of the flow (intrinsic frequency $\geq |f|$). An internal wave continuum, generated by weakly nonlinear interactions between internal gravity waves, is also present at small scales [O(0.1–10) km] and superinertial intrinsic frequencies ($\gg |f|$; Garrett and Munk 1972; Olbers et al. 2020; Dunphy and Lamb 2014). Note that, in the Earth reference frame, the frequency of internal gravity waves can be strongly modified via Doppler shifting by the low-frequency background circulation (Bretherton and Garrett 1968; Kunze 1985). Internal gravity waves can therefore span all frequencies in the Earth reference frame (extrinsic frequency), rendering their identification difficult (Shakespeare et al. 2021). Lee waves have a null extrinsic frequency by definition, and represent a special case of low-frequency internal gravity waves in the Earth reference frame. The dynamics of internal gravity waves are commonly referred to as "unbalanced" in the literature, by contrast to low-frequency, near-geostrophically-balanced mesoscale eddies. However, this terminology is not accurate for all dynamical regimes, because submesoscale currents have a significant ageostrophic (unbalanced) component as well (McWilliams 2016; Taylor and Thompson 2022).

The contribution of internal gravity waves to near-surface turbulence is not well understood. Internal gravity waves, in particular near-inertial waves, have been demonstrated to enhance the forward turbulent cascade (Polzin 2010; Whitt and Thomas 2015; Barkan et al. 2017; Rocha et al. 2018; Thomas and Arun 2020; Thomas and Daniel 2021; Barkan et al. 2021). A recent study suggested a more nuanced view, however, by showing that interactions between mesoscale eddies and internal gravity waves can result in both KE gain and loss for the eddies (Cusack et al. 2020). The possible contribution of bottom-generated lee waves to near-surface submesoscale turbulence, via interactions with other motions, has not yet been investigated to our knowledge, and is less certain (Baker and Mashayek 2021, 2022).

In summary, our current understanding of the contributions of submesoscale currents and internal gravity waves to the near-surface turbulent KE cascade at the submesoscale is incomplete. Previous studies have provided a partial characterization of the contributions of different motions to the turbulent KE cascade. They have either not distinguished the contributions of internal gravity waves from submesoscale currents and fully attributed near-surface turbulence to submesoscale currents (Sasaki et al. 2017; Dong et al. 2020; Schubert et al. 2020; Naveira Garabato et al. 2022), or they have focused solely on either internal gravity waves (Barkan et al. 2021) or submesoscale currents (Srinivasan et al. 2023). In addition, previous studies have usually explained the contributions of the different motions to the turbulent KE cascade in terms of their governing dynamics (Boyd 1992; Callies and Ferrari 2013; Srinivasan et al. 2023)—i.e., partitioning into dynamical components (geostrophic versus ageostrophic)—but have not addressed the practical issue of spatiotemporal resolution of motions. The relatively small spatiotemporal scales of the submesoscale range ($L \sim 0.1$–10 km; $T \sim$ hours–day) have long represented a technical challenge for investigations of submesoscale turbulence (McWilliams 2016). This near-surface turbulence has been documented using high-resolution numerical simulations and, to a lesser extent, with in situ observations. Characterizing how the contributions of different motions to submesoscale turbulence vary with spatiotemporal resolution has direct implications for ocean study strategies and for fundamental understanding of ocean dynamics. It is thus important to determine the scales that must be captured in order to 1) diagnose accurately the properties of near-surface submesoscale turbulence and 2) represent the effects of such turbulence on the larger-scale ocean circulation. Unanswered questions on near-surface submesoscale turbulence include: what class of motions, among submesoscale currents and internal gravity waves, contributes the most to the submesoscale turbulent KE cascade? Which turbulent cascade, inverse or forward, do such motions contribute to and why? How do these cascade contributions partition across spatiotemporal scales?

Here, we attempt, for the first time to our knowledge, to characterize the physics governing the spatiotemporal scales of near-surface turbulence in the Southern Ocean (specifically, in the Drake Passage region; Fig. 1). In this paper, the term submesoscale turbulence refers specifically to turbulence at the ocean near-surface. We first assess the contributions of submesoscale currents and internal gravity waves to the turbulent KE cascade at the submesoscale, and we then quantify their contributions in terms of dynamically relevant properties (such as governing dynamics: geostrophic versus ageostrophic, and spatiotemporal scales). To do so, we explicitly separate the two classes of motions using a high-resolution numerical simulation of the Drake Passage in winter (Fig. 1), a region and time of intense near-surface turbulence. The Drake Passage hosts an energetic mesoscale eddy field (Chelton et al. 2011); a vigorous near-surface turbulence field in winter, as indicated by the pronounced seasonality of the mixed layer depth (Dong et al. 2008) and submesoscale turbulent cascade (Qiu et al. 2014; Sasaki et al. 2014; Uchida et al. 2017; Dong et al. 2020; Schubert et al. 2020); and an intense lee wave field (Nikurashin and Ferrari 2011; Baker and Mashayek 2022). The Drake Passage is a particularly relevant region for investigating upper-ocean submesoscale turbulence—and its potential impact on the mesoscale eddy reservoir—because it has been identified as a hotspot of eddy-induced meridional overturning and transfer of climatically important tracers (Thompson and Naveira Garabato 2014; Tamsitt et al. 2017).

The remainder of this article is organized as follows. The regional numerical simulation is presented in section 2a. The separation of motions and diagnostics of the turbulent KE cascade are presented in sections 2b and 2c, respectively. Winter near-surface motions and their contributions to submesoscale turbulence are characterized in sections 3 and 4. The sensitivity of near-surface submesoscale turbulence to spatiotemporal resolutions is assessed in section 5. Our results are summarized, and their implications for observational and modeling strategies are discussed, in section 6.

2. Methodology

This section presents the data, offline processing approaches, and diagnostics used in this study. We first describe the numerical simulation of the Drake Passage. We then present the offline processing that separates submesoscale nonwave currents (NWCs) from internal gravity waves (IGWs). We finally describe the diagnostic of cross-scale KE flux used to infer the turbulent KE cascade.

a. Numerical simulation

Here we present the regional numerical simulation of the Drake Passage. We first outline the numerical setup and then assess the modeled near-surface ocean characteristics against observations.

1) NUMERICAL SIMULATION SETUP

We use a regional numerical simulation of the Drake Passage to investigate the winter near-surface turbulent KE cascade in the submesoscale range (Fig. 1). The simulation is based on a hydrostatic and Boussinesq configuration of the Massachusetts Institute of Technology general circulation model (MITgcm) (Marshall et al. 1997) and is presented in detail in Mashayek et al. (2017) and Baker and Mashayek (2022).

The simulation has an average horizontal resolution of $dx \sim 1$ km (1/100°), which corresponds to an effective resolution of about 5 km (the wavenumber KE spectrum shows a break in slope and departs from the typical power law of the submesoscale turbulent regime (k^{-2}; Callies and Ferrari 2013) at a horizontal scale of around 5 km; Fig. 6a). In the vertical, 225 depth levels are distributed at intervals ranging from $dz = 10$ m at the surface, $dz = 25$ m between 600 and 4555 m, to $dz = 62$ m at the maximum depth.

A nesting approach is used to set up the simulation. The simulation is nested within a lower-resolution simulation ($dx = 1/20°$ and 100 vertical levels) of a larger region of the Southern Ocean described in Tulloch et al. (2014). Initial and boundary conditions are provided by the lower-resolution parent simulation. A restoring condition toward the parent simulation is applied with a 4-h time scale at the grid boundaries through a sponge layer of 1° width. Surface forcing is taken from the ERA-Interim reanalysis (Simmons 2006) with a 6-h time scale. Wind stress is calculated from bulk formula using the relative atmosphere–ocean velocities. The wind forcing therefore accounts for wind fluctuations due to oceanic flows ranging from large-scale down to the horizontal resolution of the simulation ($dx \sim 1$ km). No tidal forcing is used in the simulation. Vertical mixing is applied through background values of vertical diffusivity and viscosity of 5×10^{-5} m^2 s^{-1}. Intense vertical diffusivity and viscosity, due to unresolved shear and convective instabilities, are represented by the K-profile parameterization (Large et al. 1994), with the critical Richardson number for shear instability set to $\mathrm{Ri}_c = 0.33$.

The parent simulation is run over 3 years, and the $dx \sim 1$ km simulation is run for about 3 months (July–September). This study is based on the final 30 days of the $dx \sim 1$ km simulation (September). Numerical output was saved as hourly snapshots and hourly averages. Analyses presented in sections 2–4 are based on hourly averages, and outputs with coarser temporal resolutions are used in section 5.

2) OBSERVED AND MODELED OCEAN DYNAMICS

Several characteristics of the modeled ocean dynamics in the Drake Passage have been assessed against observations, in the context of larger parent numerical simulations (Tulloch et al. 2014; Mashayek et al. 2017) and of our numerical simulation (Baker et al. 2023). At the surface, the modeled surface hydrography and eddy KE were validated against satellite altimetry data (Tulloch et al. 2014). Across the water column, the impact of mesoscale dynamics on diapycnal mixing was accurately simulated (Mashayek et al. 2017). At the bottom, the water mass characteristics and distribution were validated against in situ observations (Baker et al. 2023).

Here, we show that our numerical simulation is a plausible realization of the near-surface dynamics of the Drake Passage region. We assess the modeled near-surface dynamics by comparing the modeled winter stratification and mixed layer depth against Argo data (Kolodziejczyk et al. 2021; Holte et al. 2017) and *World Ocean Atlas 2018* (*WOA18*) climatology (Locarnini et al. 2018; Zweng et al. 2019) (Fig. 2). Stratification and mixed layer depth result from the competition of several processes driven by buoyancy and momentum atmospheric forcings, and which are partially resolved and parameterized in our model. The two fields, therefore, provide a measure of the integrated near-surface dynamics. We additionally evaluate the modeled near-surface KE partitioning across horizontal scales as represented in our simulation against the one used in Rocha et al. (2016).

(i) Near-surface stratification

Temporally and spatially averaged vertical profiles of modeled and observed stratification are shown at the near-surface in Fig. 2a. The modeled stratification (mean: 2.65×10^{-6} s^{-2}; standard error: 1.15×10^{-7} s^{-2}) falls within the range of Argo profiles (mean: 5.14×10^{-6} s^{-2}; standard error: 4.10×10^{-6} s^{-2})—representing the variability of stratification in the region—and is in reasonably good agreement with Argo-based and *WOA18* climatologies.

The near-surface ocean (0–300-m depth) is slightly less stratified in the model than in observations. Mimicking the Argo sampling in the model improves the agreement with observations at depths > 100 m, with very good agreement at depths greater than 250 m. The slight differences in stratification would suggest an imbalance between processes restratifying (submesoscale processes including mixed layer baroclinic instability; Haine and Marshall 1998; Boccaletti et al. 2007; Fox-Kemper et al. 2008) and destratifying [vertical mixing induced by internal waves (Song et al. 2019) and parameterized using the K-profile parameterization (Large et al. 1994)] the winter near-surface ocean at depths < 100 m. However, the differences between the model and observations at depths < 100 m (averaged difference of 3.87×10^{-6} s^{-2}) are smaller than the standard error of stratification shown by the Argo profiles (4.10×10^{-6} s^{-2}).

(ii) Mixed layer depth

The mixed layer is a characteristic feature of the near-surface ocean. It corresponds to a quasi-uniform density layer extending from the ocean surface to $O(10–100)$ m. Its depth is shaped by atmospherically forced processes working for or against the mixed layer stratification, and it varies seasonally and between oceanic regions.

A monthly Argo-based global climatology of the mixed layer depth uses a hybrid method of mixed layer depth estimation that combines a potential density algorithm and variable threshold values (Holte et al. 2017). We infer the mixed layer depth from our numerical simulation using a double criterion on vertical variations of potential density. This method, based on the gradients and curvature of density profiles, has the benefit of being straightforward to implement and of accurately locating sharp changes of density, such as the mixed layer base. Such a method has recently been used to revisit the characterization of subtropical mode waters in the South Atlantic and improve understanding of their formation (Chen et al. 2022).

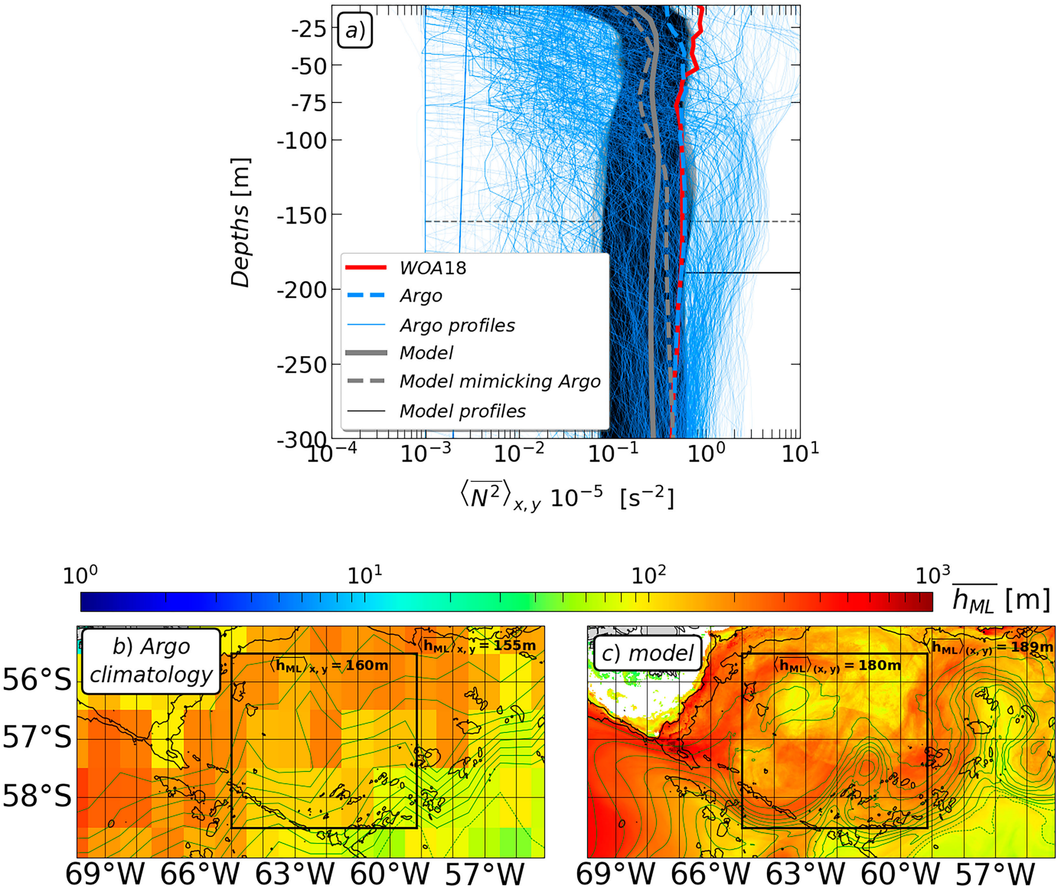

FIG. 2. Observed and modeled winter near-surface characteristics. (a) Temporally and spatially averaged stratification profiles ($\langle \overline{N^2} \rangle_{x,y}$) from Argo data and *WOA18* climatology (July–September) and our $dx \sim 1$ km model (September). Two averaged profiles are computed from our model: one accounting for the profiles at the model's spatial resolution (plain black line) and another mimicking the spatial sampling of Argo data (dashed black line). Mean mixed layer depths inferred from the Argo climatology (gray horizontal line) and the model (black horizontal line) are shown. Time-averaged mixed layer depth ($\overline{h_{\mathrm{ML}}}$) from (b) Argo monthly climatology (July–September; Holte et al. 2017) and (c) $dx \sim 1$ km model (September). Black contours show 1000- and 3000-m isobaths and the black square denotes the subregion of spatially averaged $\langle \cdot \rangle_{(x,y)}$. Green contours show isolines of time-averaged potential temperature at the surface from $-1°$ to 5°C with an interval of 0.5°C for Argo climatology (July–September; Holte et al. 2017) averaged in the mixed layer in (b) and our model at the surface in (c).

Temporally averaged winter mixed layer depths from the Argo climatology (July–September) and our model (September) are shown in the region of the Drake Passage (Figs. 2b,c). Modeled and observed mixed layer depths exhibit patterns and magnitudes in fairly good agreement, with a typical deep winter mixed layer [$O(>100)$ m] in most of the domain. The mixed layer displays contrasting depths between two areas separated by the Subantarctic Front, located along the West Scotia Ridge, where isotherms of potential temperature exhibit large gradients (green isolines in Figs. 2b,c). The mixed layer is deep [$O(>100)$ m] on the warm side of the front (northwest of the ridge) and shallower [$O(<100)$ m] on the cool side of the front (south of the ridge).

Modeled winter mixed layer depths have magnitudes somewhat larger than observed. The model overestimates the mixed layer depth when averaged over the full domain by 25%, and by 12.5% when averaged over a central subdomain (squared subdomain shown in Figs. 2b,c). Deeper modeled mixed layers are consistent with the modeled stratification being biased low compared to observations (Fig. 2a). The differences can also be partially explained by the distinct methods used to infer the mixed layer depth from observations and the model. This is consistent with the findings of Holte et al. (2017) who, in regions of deep mixed layers, reported differences of about 10% between the mixed layer depth inferred from hybrid and variable threshold value methods. The differences may also be influenced by the distinct modeled (30 days) and observed (>10 years) time series.

(iii) *Horizontal wavenumber spectrum of KE*

Temporally averaged near-surface horizontal wavenumber spectra of KE computed in the Drake Passage region are compared between the global llc4320 simulation ($dx \sim 5$ km, including 6-hourly atmospheric forcing and a tidal forcing) and our numerical simulation ($dx \sim 1$ km, including 6-hourly atmospheric forcing and no tidal forcing) [Fig. 8d in Rocha et al. (2016) and Fig. 6a in this study]. The characteristics of the two near-surface horizontal wavenumber KE spectra are partially consistent. Figure 8d of Rocha et al. (2016) shows the surface horizontal wavenumber KE spectrum for the winter period (September–December). The maximum of KE is found at about 150 km, and KE decreases from the mesoscale to the submesoscale range (100–10 km) with a power law between −3 and −2. Figure 6a shows the near-surface (averaged in the layer 0–100 m) horizontal wavenumber KE spectrum for the winter period (September). No maximum of KE is visible in the horizontal range of 150–3 km, which supports a maximum of KE at scales larger than 150 km as shown by Rocha et al. (2016). KE decreases in the 100–10-km range with a power law of −2 (the spectral slope is fairly uniform across the near-surface (0–100 m; not shown). The flatter spectral slope in our simulation compared to the llc4320 simulation goes along with a larger KE magnitude at all horizontal scales.

The reasonably good agreement between modeled and observed estimates of time-averaged stratification, mixed layer depth, and between modeled horizontal wavenumber KE spectra—considering the different methods and data—indicates that our model is a plausible realization of the dynamics of the Drake Passage. Our model is therefore suitable for investigating winter near-surface turbulence.

b. *Separation of classes of motions*

In this subsection, we present our offline processing, which combines a Lagrangian filter and Helmholtz decomposition to 1) separate the flow into two classes of motions (NWC versus IGW) and 2) assess their governing dynamics (rotational versus divergent).

1) LAGRANGIAN FILTER: NWCS AND IGWS

Velocity fields are analyzed offline using a Lagrangian filter to represent them as the sum of components associated with nonwave currents—including submesoscale currents—and internal gravity waves (Shakespeare et al. 2021; Bachman et al. 2022; Baker and Mashayek 2022; Cutolo et al. 2022; Rama et al. 2022b,a). See appendix A for details of the Lagrangian filtering performed on our model output. The separation of internal waves from other oceanic flows is a long-standing issue in oceanography, and different methods are documented (Shakespeare et al. 2021). Here, we discuss the challenges represented by such a separation and our choice of using Lagrangian filtering.

The identification and separation of internal waves ($100\,\mathrm{km} \gtrsim L \gtrsim 1\,\mathrm{km}$; $T \leq T_f$ in the reference frame of the flow, with $T_f = 2\pi/f = 14\,\mathrm{h}$ being the period of the inertial frequency f in the Drake Passage) from submesoscale currents ($\lambda_{\mathrm{Rd}} = 75\,\mathrm{km} \gtrsim L \gtrsim 0.1\,\mathrm{km}$; day $\gtrsim T \gtrsim$ hours, with λ_{Rd} the Rossby deformation wavelength in the Drake Passage) is challenging. The two classes of motions have overlapping dynamics, with a significant ageostrophic part. As a result, a separation method based on a dynamical criterion (Bühler et al. 2014) is inadequate. The two flow types have overlapping spatiotemporal scales in the Earth reference frame too. They share a range of horizontal scales, and the characteristic time scale of internal waves can be strongly modified by the flow in which they propagate (Bretherton and Garrett 1968; Kunze 1985). Internal waves can be advected and trapped by the low-frequency background circulation, resulting in a Doppler-shifted extrinsic frequency lower than the intrinsic frequency, and comparable to that of nonwave currents. This phenomenon has been shown to alter the spatiotemporal scales of internal gravity waves in regions of intense mean currents and mesoscale eddy field (Jones et al. 2023). Torres et al. (2022) proposed a separation method based on the vertical structure of submesoscale currents and internal waves that bypasses this issue. However, this method was developed in a region of upwelling with a specific stratification profile, such that the validity of a vertical separation scale cannot readily be generalized.

The Lagrangian filter is a generic method allowing us to sidestep overlapping scales between submesoscale currents and internal waves for any dynamical regime (Shakespeare et al. 2021). By performing a temporal filter on Lagrangian velocities, we make use of the existence of a separation time scale (T_f) between submesoscale currents ($T \geq T_f$) and internal waves ($T \leq T_f$) in the frame of the flow (Polzin and Lvov 2011). The Lagrangian filter has been shown to isolate internal waves successfully in high-resolution numerical simulations, including low-frequency internal waves such as lee waves, which experienced a sufficient Doppler shift to have an intrinsic frequency greater than the inertial frequency (Shakespeare et al. 2021; Baker and Mashayek 2022).

We refer henceforth to the filtered modeled velocity fields as nonwave currents and internal gravity waves. IGW motions account for any flows of high intrinsic frequency. These encompass the bulk of near-inertial motions and internal waves. However, submesoscale fronts and internal waves are inherently related, and their separation may be unclear in some dynamical regimes. Internal waves are known to initiate frontogenesis, and submesoscale fronts can radiate internal waves (Alford et al. 2013; Vanneste 2013; Nagai et al. 2015; Shakespeare and Hogg 2017). Such submesoscale fronts, of high intrinsic frequency, would therefore be classified in the IGW component with the Lagrangian filtering approach. We expect such high-frequency fronts not to be dominant in our numerical simulation ($dx \sim 1$ km). We find that the modeled NWC and IGW motions account, respectively, for the bulk of submesoscale currents and internal gravity waves in appendix A, using a statistical analysis of vorticity and strain fields and frontogenetic tendency (Figs. A1 and A2).

An advantage of the offline Lagrangian filter is that it enables the separation of motions regardless of their generation mechanism. This is important for internal gravity waves in particular, because even though they are mostly forced by atmospheric drivers, they can also be generated by topographic interactions (De Marez et al. 2020; Baker and Mashayek 2021) or be spontaneously generated (Alford et al. 2013; Vanneste 2013; Nagai et al. 2015; Shakespeare and Hogg 2017). This offline approach may therefore allow a more exhaustive characterization of the contribution of internal gravity waves to the near-surface turbulent KE cascade than methods using varying atmospheric forcing to discriminate one class of motions (Barkan et al. 2021; Srinivasan et al. 2023).

2) HELMHOLTZ DECOMPOSITION: ROTATIONAL AND DIVERGENT MOTIONS

Horizontal velocities of NWC and IGW motions are further decomposed offline into the sum of rotational and divergent components by applying a Helmholtz decomposition. See appendix B for details of the Helmholtz decomposition performed on our model output. This method has been used to decompose the flow approximately into geostrophic (balanced) and ageostrophic (unbalanced) parts (Molemaker et al. 2010; Gula et al. 2014; Torres et al. 2018; Bühler et al. 2014; Srinivasan et al. 2023). Rotational and divergent velocities form a unique decomposition at each point of the domain. Thus, we write:

$$\mathbf{u}(x, y) = \underbrace{\nabla_H \times \psi\mathbf{k}}_{\text{rotational } \mathbf{u}} + \underbrace{\nabla_H \phi}_{\text{divergent } \mathbf{u}}, \tag{1}$$

with $\mathbf{u} = (u, v)$ as the horizontal velocity vector, ψ and ϕ respectively denoting the velocity streamfunction and potential, $\nabla_H = (\partial_x, \partial_y, 0)$ as the horizontal gradient operator, and $\mathbf{k} = (0, 0, 1)$ the vertical unit vector. Rotational velocities derive from a streamfunction (ψ) and are horizontally divergence-free. Divergent velocities derive from a potential (ϕ) and are two-dimensionally irrotational. Thus, for the NWC flows, rotational and divergent velocities respectively account for the geostrophically balanced and ageostrophic (unbalanced) parts of the flows.

We use the Helmholtz decomposition to assess the partitioning of NWC and IGW motions into dynamical components, and thereby assess their governing dynamics. Both NWC and IGW motions have significant rotational and divergent components, as shown from near-surface normalized relative vorticity [$\zeta/f = (1/f)\nabla_H^2\psi$] and divergence [$\delta/f = (1/f)\nabla_H^2\phi$] at a given time step (Fig. A1). Mesoscale and submesoscale eddies are primarily in geostrophic balance and will mainly project onto the rotational component (Gill 1982; Stone 1970). Submesoscale fronts are partially geostrophically balanced and significantly contribute to rotational and divergent components (McWilliams 2016; Taylor and Thompson 2022). Indeed, fronts undergoing frontogenesis can be decomposed into a primary alongfront circulation in thermal wind balance, and a secondary cross-front ageostrophic circulation (McWilliams 2016, 2021). In the context of the Helmholtz decomposition, the alongfront and cross-front frontogenetic circulations are respectively approximated by the rotational and divergent components of fronts. The partitioning of internal gravity waves has been explicitly derived in the context of stratified turbulence, and is predicted to vary with respect to wavenumber and frequency (Bartello 1995). The partitioning of NWC and IGW varies seasonally. Torres et al. (2018) showed that submesoscale currents are largely rotational and have a significant divergent component in winter. Internal gravity waves have both significant rotational and divergent parts. We characterize the partitioning of the modeled winter NWC and IGW motions into dynamical components in sections 3a and 3b (Figs. 3–5).

In summary, our approach leads to the definition of four categories of horizontal velocities: NWC rotational, NWC divergent, IGW rotational, and IGW divergent. The initial velocity field is recovered by summing the four categories of velocities.

c. Cross-scale kinetic energy flux

Turbulent KE cascades are inferred from the horizontal cross-scale KE flux, computed using a coarse-graining method with respect to spatial scale (Aluie et al. 2018; Schubert et al. 2020; Srinivasan et al. 2023). Note that we do not consider the contribution of vertical cross-scale KE flux to the turbulent KE cascades here, which could be significant for internal gravity waves and lee waves in particular. The coarse-graining method is based on a low-pass spatial filtering function, and allows inference of the KE flux across a given spatial scale l in physical space. The cross-scale KE flux, $\overline{\Pi}^l(x, y)$ [Eq. (2)], measures the KE transfer from scales $> l$ to scales $< l$ caused by nonlinear interactions:

$$\overline{\Pi}^l(x, y) = -\frac{1}{2}[\nabla_H \overline{\mathbf{u}}^l + (\nabla_H \overline{\mathbf{u}}^l)^{\mathrm{T}}] : (\overline{\mathbf{uu}}^l - \overline{\mathbf{u}}^l\overline{\mathbf{u}}^l), \tag{2}$$

$$\begin{aligned}\overline{\Pi}^l(x, y) = & -\underbrace{\frac{1}{2}(\partial_x\overline{u}^l + \partial_y\overline{v}^l)(\overline{uu}^l - \overline{u}^l\overline{u}^l + \overline{vv}^l - \overline{v}^l\overline{v}^l)}_{\text{convergence contribution}} \\ & - \underbrace{(\partial_y\overline{u}^l + \partial_x\overline{v}^l)(\overline{uv}^l - \overline{u}^l\overline{v}^l)}_{\text{shear strain contribution}} \\ & + \underbrace{\frac{1}{2}(\partial_x\overline{u}^l - \partial_y\overline{v}^l)(\overline{vv}^l - \overline{v}^l\overline{v}^l - \overline{uu}^l + \overline{u}^l\overline{u}^l)}_{\text{normal strain contribution}},\end{aligned} \tag{3}$$

with $\overline{(\cdot)}^l$ denoting the low-pass filter at the cutoff spatial scale l and the colon denoting the tensor inner product leading to a scalar. See appendix C for details of the computation of the cross-scale KE flux in our model. The sign of $\overline{\Pi}^l(x, y)$ indicates the direction of the KE transfer. Negative values correspond to an upscale KE transfer and indicate an inverse turbulent cascade. Positive values correspond to downscale KE transfer and indicate a forward turbulent cascade.

To assess the contributions of NWC and IGW motions to submesoscale turbulence, we calculate the cross-scale KE flux for the different categories of velocity fields (NWC rotational, NWC divergent, IGW rotational, and IGW divergent). The different cross-scale KE flux account for the KE flux caused by nonlinear interactions within individual classes of motions, and between the different classes of motions. The four categories of velocity fields, resulting from the offline processing, describe four individual classes of motions and are not coupled per se. The coupling (interaction) between the classes of motions comes from the cross-scale KE flux being a nonlinear term. For example, the cross-scale KE flux for total NWC motions, $\overline{\Pi}^l_{\text{NWC}} = \overline{\Pi}^l_{\text{NWC\_rot}} + \overline{\Pi}^l_{\text{NWC\_div}} + \overline{\Pi}^l_{\text{NWC\_rot–div}}$, is expressed as the sum of the individual contributions of NWC rotational motions ($\overline{\Pi}^l_{\text{NWC\_rot}}$) and NWC divergent motions

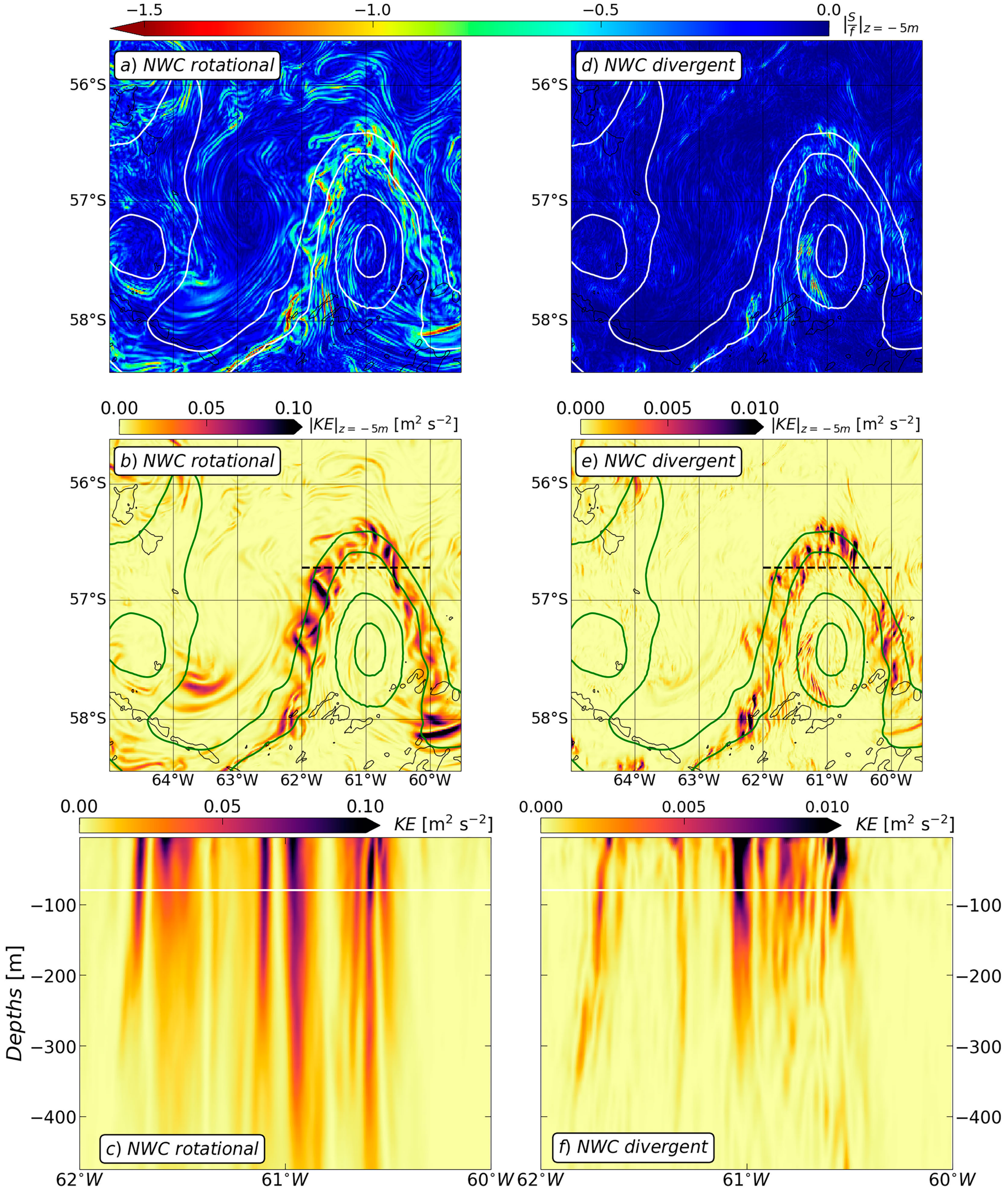

FIG. 3. Spatial structure of submesoscale NWC (left) rotational and (right) divergent motions ($L < \lambda_{\rm Rd} \sim 75$ km; $T > 1$ day). Near-surface horizontal sections of (a),(d) normalized strain and (b),(e) KE, and (c),(f) vertical sections of KE [at 56.81°S shown with black dotted line in (b) and (e)] for NWC rotational and divergent motions in the left and right panels, respectively. In (a), (b), (d), and (e), the 0.25-, 0.5-, 0.75-, and 1-m isolines of time-averaged sea surface height are shown in white and green contours, and 1000- and 3000-m isobaths are shown in black contours. Mean mixed layer depth is shown in white in (c) and (f). Fields are plotted at a time step in the subregion denoted in Fig. 2.

($\overline{\Pi}^l_{\rm NWC\_div}$), plus a coupling term between the two types of motions ($\overline{\Pi}^l_{\rm NWC\_rot\text{–}div}$).

The main cross-scale KE flux caused by individual classes of motions considered in this study (section 4) include (i) $\overline{\Pi}^l_{\rm rot\text{–}rot}$, accounting for interactions between nonseparated (NWC plus IGW) rotational motions; (ii) $\overline{\Pi}^l_{\rm NWC\text{–}NWC}$, for interactions between NWC total (rotational plus divergent) motions; (iii) $\overline{\Pi}^l_{\rm NWC\_rot\text{–}NWC\_rot}$, for interactions between NWC rotational motions; and (iv) $\overline{\Pi}^l$, for interactions inferred from the nonseparated (NWC plus IGW) total (rotational plus divergent) modeled velocities. These individual cross-scale KE fluxes are explicitly computed by substituting in Eq. (2) the

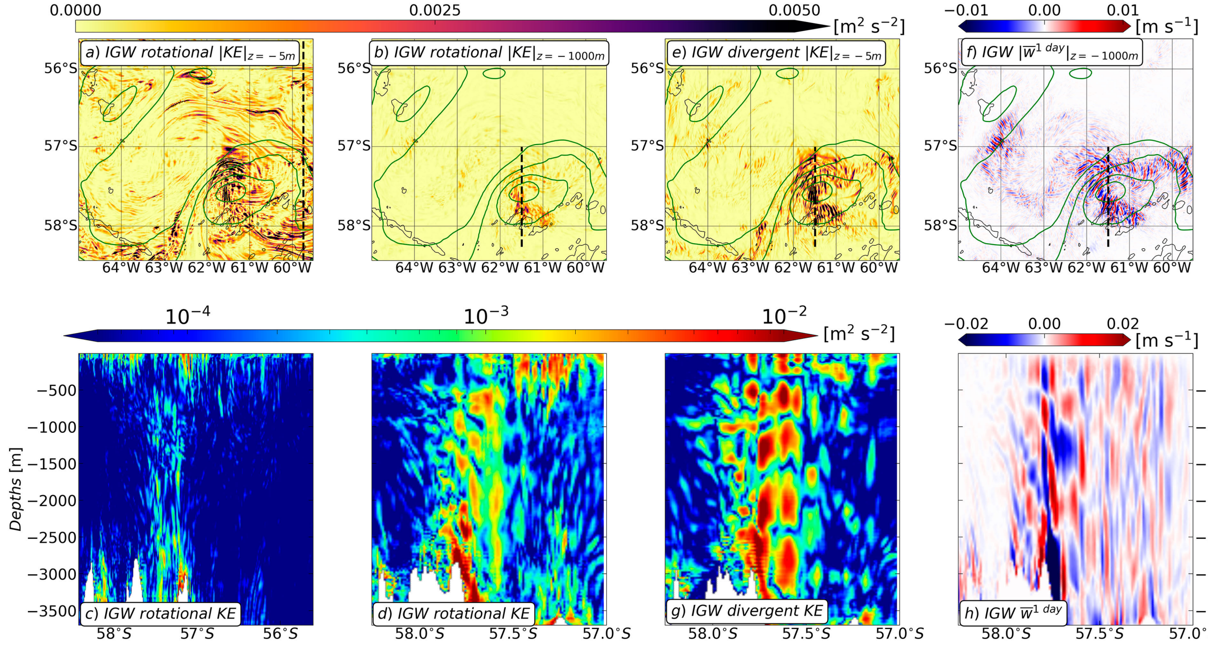

FIG. 4. Spatial structure of IGW (a)–(d) rotational and (e)–(h) divergent motions. Horizontal sections of rotational KE at two depths [near-surface in (a) and 1000-m depth in (b)] and vertical sections of rotational KE for two vertical IGW structures [(c) depicts the section of surface-intensified structures shown in (a); (d) depicts the section of deep-reaching structures shown in (b)]. Horizontal sections of (e) near-surface divergent KE and (f) daily-averaged vertical velocity at 1000-m depth, and (g),(h) their vertical sections along the section crossing deep reaching structures shown in (e) and (f). In (a), (b), (e), and (f), green contours show 0.25-, 0.5-, 0.75-, and 1-m isolines of time-averaged sea surface height, and black contours show 1000- and 3000-m isobaths. Fields are plotted at a time step [except for the daily averages in (f) and (h)] in the subregion shown in Fig. 2.

velocity field of the motions considered. The main cross-scale KE flux caused by the coupling between two classes of motions considered in this study (section 4) include (i) $\overline{\Pi}^{l}_{\text{rot–div}}$, accounting for interactions between nonseparated (NWC plus IGW) rotational and divergent motions; (ii) $\overline{\Pi}^{l}_{\text{NWC\_rot–NWC\_div}}$, for interactions between NWC rotational and divergent motions; (iii) $\overline{\Pi}^{l}_{\text{NWC–IGW}}$, for interactions between NWC and IGW total (rotational plus divergent) motions; and (iv) $\overline{\Pi}^{l}_{\text{NWC\_rot–IGW\_rot}}$, for interactions between NWC and IGW rotational motions. The coupled cross-scale KE flux are as follows:

$$\overline{\Pi}^{l}_{A-B}(x, y) = -[\nabla_H \overline{\mathbf{u}}_A^{l} + (\nabla_H \overline{\mathbf{u}}_A^{l})^{\mathrm{T}}] : \left[\frac{1}{2}(\overline{\mathbf{u}_B\mathbf{u}_B}^{l} - \overline{\mathbf{u}}_B^{l}\overline{\mathbf{u}}_B^{l}) + (\overline{\mathbf{u}_A\mathbf{u}_B}^{l} - \overline{\mathbf{u}}_A^{l}\overline{\mathbf{u}}_B^{l})\right]$$
$$- [\nabla_H \overline{\mathbf{u}}_B^{l} + (\nabla_H \overline{\mathbf{u}}_B^{l})^{\mathrm{T}}] : \left[\frac{1}{2}(\overline{\mathbf{u}_A\mathbf{u}_A}^{l} - \overline{\mathbf{u}}_A^{l}\overline{\mathbf{u}}_A^{l}) + (\overline{\mathbf{u}_A\mathbf{u}_B}^{l} - \overline{\mathbf{u}}_A^{l}\overline{\mathbf{u}}_B^{l})\right] \tag{4}$$

with A and B representing any category of horizontal velocity, defined in section 2b(2), with the condition that $A \neq B$. In practice, the different coupled cross-scale KE flux are calculated as residuals based on the following relationships:

$$\overline{\Pi}^{l}_{\text{rot–div}} = \overline{\Pi}^{l} - \overline{\Pi}^{l}_{\text{rot}} - \overline{\Pi}^{l}_{\text{div}}, \tag{5}$$

$$\overline{\Pi}^{l}_{\text{NWC–IGW}} = \overline{\Pi}^{l} - \overline{\Pi}^{l}_{\text{NWC}} - \overline{\Pi}^{l}_{\text{IGW}}, \tag{6}$$

$$\overline{\Pi}^{l}_{\text{NWC\_rot–IGW\_rot}} = \overline{\Pi}^{l}_{\text{rot}} - \overline{\Pi}^{l}_{\text{NWC\_rot}} - \overline{\Pi}^{l}_{\text{IGW\_rot}}, \tag{7}$$

$$\overline{\Pi}^{l}_{\text{NWC\_rot–NWC\_div}} = \overline{\Pi}^{l}_{\text{NWC}} - \overline{\Pi}^{l}_{\text{NWC\_rot}} - \overline{\Pi}^{l}_{\text{NWC\_div}}. \tag{8}$$

The coupling between the different classes of motions includes a unique cross-scale KE flux term:

$$\overline{\Pi}^{l}_{\text{NWC\_(rot–div)–IGW\_(rot–div)}} = \overline{\Pi}^{l}_{\text{NWC–IGW}} - \overline{\Pi}^{l}_{\text{NWC\_rot–IGW\_rot}} - \overline{\Pi}^{l}_{\text{NWC\_div–IGW\_div}}. \tag{9}$$

This term represents the interactions between the four different classes of motions. It must not be mistaken for the net cross-scale KE flux ($\overline{\Pi}^{l}$), represented by the nonseparated (NWC plus IGW) total (rotational plus divergent) velocities, which includes interactions within and across individual classes of motions.

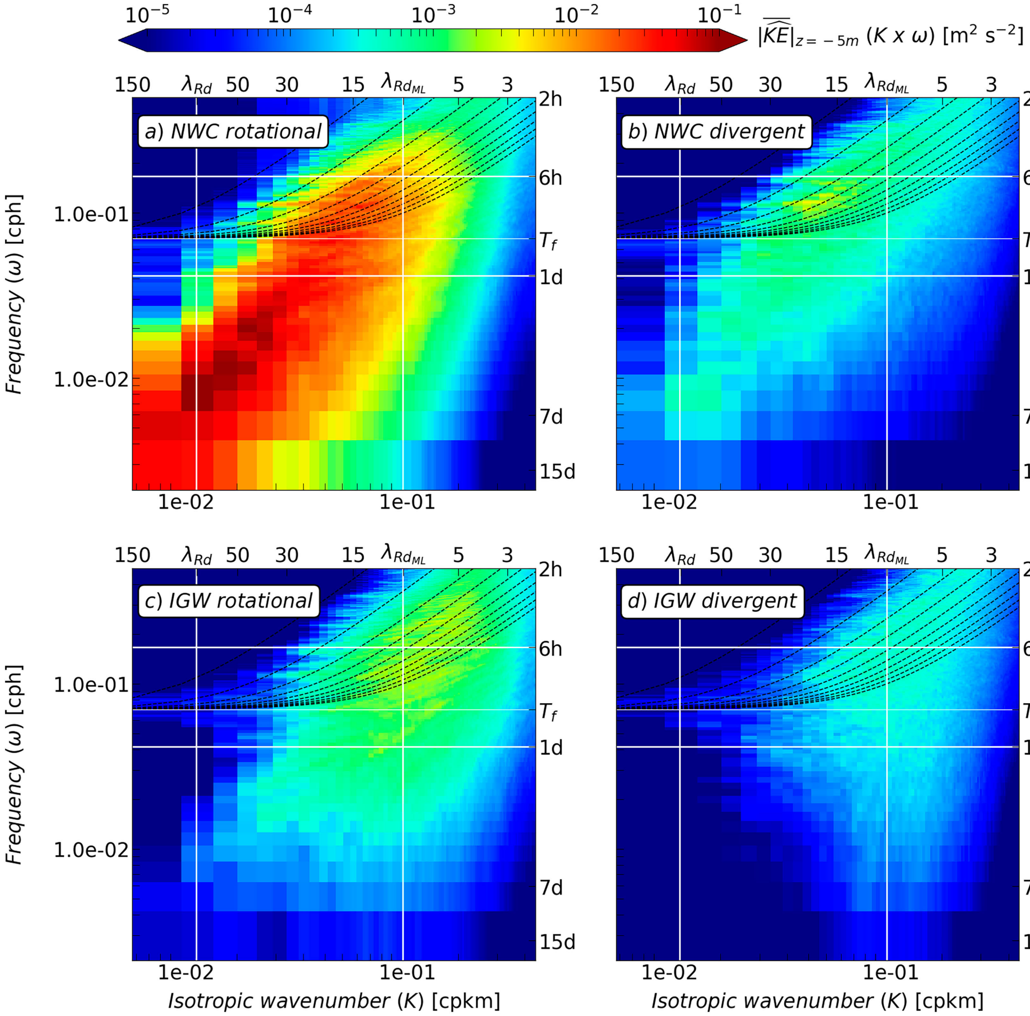

FIG. 5. Spatiotemporal scales of winter NWC and IGW motions. Frequency–horizontal wavenumber spectra in the Earth reference frame of near-surface KE for NWC (a) rotational and (b) divergent components and IGW (c) rotational and (d) divergent components. Note that the spectra are in variance-preserving form. Black dotted lines show internal gravity waves modal dispersion relationships (1st–10th vertical modes) computed for a stratification value diagnosed at the base of the mean mixed layer depth (200-m depth). White lines show characteristic spatiotemporal scales.

3. Winter motions in the submesoscale range

In this section, we characterize the NWC and IGW motions present in the winter near-surface ocean at the submesoscale. We first describe their governing dynamics and spatial structure in physical space. We then assess their spatiotemporal scales.

a. Description in physical space

1) NONWAVE CURRENTS

NWC rotational and divergent motions in the submesoscale range (λ_{Rd} = 75 km > L with λ_{Rd} the Rossby deformation wavelength in the Drake Passage) are represented in physical space at a given time step, with near-surface horizontal sections of normalized strain (S/f) and KE, as well as vertical sections of KE (Fig. 3). Submesoscale NWC velocities are determined using a combination of spatial and temporal filtering. NWC velocities are high-pass filtered in time (cutoff frequency of 1 day) and space (smoothing scale of 50 km, just below λ_{Rd} = 75 km).

NWC motions in the submesoscale range correspond to primarily rotational eddies and to fronts including a rotational and a divergent components (Figs. 3 and A1). Rotational fronts have larger-scale spatial structures than divergent fronts, and are the most energetic. They correspond to meandering and elongated surface-intensified fronts, extending well beyond the mixed layer base in the vertical.

A significant fraction of frontal areas—defined by the |0.5| contour of normalized strain—have values of normalized strain exceeding 1 (rotational 12%, and divergent 7%; from orange to red values in Figs. 3a,d). This indicates that fronts have short temporal scales, down to shorter than the inertial period in the Earth reference frame ($T < 1/f$). This corroborates the need for Lagrangian filtering to separate submesoscale currents (NWC motions) from internal gravity waves (IGW motions). The short temporal scales of submesoscale fronts ($T < 1/f$) have been previously documented (Gula et al. 2014; Torres et al. 2022).

2) INTERNAL GRAVITY WAVES

IGW rotational and divergent motions in the submesoscale range ($\lambda_{\mathrm{Rd}} = 75$ km $> L$) are represented in physical space at a given time step with horizontal and vertical sections of KE and daily-averaged vertical velocity (Fig. 4). IGW motions present in our numerical simulation include near-inertial motions, lee waves, and the internal wave continuum. The latter is generated by interactions between the different oceanic flows transferring KE of IGWs across spatiotemporal scales (Olbers 1976; Olbers et al. 2020; Dunphy and Lamb 2014), but note that the full internal wave continuum cannot be captured by our numerical simulation, which is hydrostatic and lacks internal tides [cf. section 2a(1)]. The internal gravity wave partitioning into rotational and divergent components has been documented in previous studies (Bartello 1995; Torres et al. 2018, 2022). Near-inertial waves and the internal wave continuum have been shown to roughly evenly partition into rotational and divergent components (Torres et al. 2018, 2022). To our knowledge, the partitioning of lee waves into dynamical components is unknown.

(i) IGW rotational motions

IGW rotational motions are consistent with a superinertial wave continuum, near-inertial waves, and low-frequency lee waves. The near-surface rotational KE shows elongated IGW trains distributed ubiquitously across the domain, in the path of or away from the mean circulation (Fig. 4a; the mean circulation is represented by green contours of time-averaged sea surface height). Most structures of the IGW train are not visible from rotational KE at 1000-m depth (Fig. 4b), suggesting that most have a surface-intensified structure. Intense values of KE are found at 1000-m depth in a specific area (62°–61°W and 57°–58°S), located in the path of the mean circulation (green contours) and in the vicinity of topographic roughness (black isobaths), suggesting that there are IGW motions of deep-reaching vertical structure in this area.

The vertical section of rotational KE across surface-intensified IGW structures (black dotted line at 59.5°W in Fig. 4a) shows that most of the IGW trains extend through the near-surface ocean [0–$O(100)$ m] (Fig. 4c). This vertical structure is compatible with wind-generated near-inertial motions (Alford et al. 2016). This interpretation is supported by the characteristic temporal scales of the surface-intensified patterns of rotational KE. An 87% root-mean-square error is found between subinertial rotational KE ($T > T_f$; not shown) and rotational KE at the time step of Fig. 4, indicating that the surface-intensified patterns of rotational KE have superinertial frequencies.

The vertical section of rotational KE across deep-reaching IGW structures (black dotted line at 61.5°W in Fig. 4b) shows that these structures correspond to bottom-intensified patterns of rotational KE, which extend over the water column to the surface (Fig. 4d). This vertical structure is compatible with vertically propagating waves, such as lee waves (De Marez et al. 2020; Baker and Mashayek 2021).

(ii) IGW divergent motions

IGW divergent motions are primarily consistent with low-frequency lee waves. The near-surface horizontal section of divergent KE displays hatched patterns, mainly located in areas in the path of the mean circulation (Fig. 4e). The most intense values of divergent KE are collocated with the rotational KE patterns extending through the water column and consistent with lee waves (62°–61°W and 57°–58°S; Figs. 4b,d). In this area, the intense hatched patterns of near-surface divergent KE are collocated with strong low-frequency vertical velocities at 1000-m depth (Figs. 4e,f), suggesting that the two patterns are vertically extensive. This is confirmed by vertical sections, which show that the intense patterns of KE and low-frequency vertical velocity have a bottom-intensified structure, which spans through the water column to the surface (Figs. 4g,h).

The spatial correspondence between bottom-intensified patterns of rotational and divergent KE and low-frequency vertical velocities, intensified through the water column up to the surface, supports the presence of lee waves in the near-surface ocean. This suggests that lee waves might contribute to near-surface turbulence, potentially shedding new light on their role in near-surface dynamics. We discuss the possible contribution of bottom-generated lee waves to near-surface turbulence in sections 4 and 5.

In summary, submesoscale NWC motions correspond to primarily rotational eddies and fronts with rotational and divergent components. Submesoscale IGW motions primarily consist of near-inertial motions and the internal wave continuum that appear largely rotational at a given time step, as well as for lee waves with rotational and divergent components. We characterize the motions' spatiotemporal scales in the next section.

b. Description in terms of spatiotemporal scales

The spatiotemporal scales of rotational and divergent components of NWC and IGW motions are assessed with frequency–horizontal wavenumber spectra of near-surface KE in the Earth reference frame (Fig. 5). See appendix D for details of the computation of KE spectra.

1) NONWAVE CURRENTS

NWC rotational motions extend from the mesoscale, at large spatial and long temporal scales ($L \gtrsim \lambda_{\mathrm{Rd}} = 75\,\mathrm{km}; T \gtrsim \mathrm{days}$), to the submesoscale range, at intermediate spatial and temporal scales ($\lambda_{\mathrm{Rd}} = 75\,\mathrm{km} \gtrsim L > 3\,\mathrm{km}; \mathrm{day} \gtrsim T > 2\,\mathrm{h}$) (Fig. 5a). This is the most energetic class of motions of any spatiotemporal scales, consistent with a typical winter near-surface regime (Torres et al. 2022). The KE continuum of NWC rotational motions in the mesoscale and submesoscale ranges (Fig. 5a) points to the occurrence of strong nonlinear interactions that transfer KE across spatiotemporal scales.

NWC divergent motions are the most energetic in the submesoscale range, but are less energetic than NWC rotational motions of any spatiotemporal scales (Fig. 5b and ratio of rot/div; not shown). Both NWC rotational and divergent motions have a significant KE level at high frequencies ($T \leq T_f$) in the Earth reference frame, as previously inferred from the normalized strain in physical space (Figs. 3a,d).

2) INTERNAL GRAVITY WAVES

Variance-preserving frequency–wavenumber KE spectra for rotational and divergent components of IGWs are largest at small spatial scales ($L \leq 30$ km), where they form a KE continuum across low and high frequencies (7 days $> T >$ 2 h) (Figs. 5c,d). At small spatial scales and high frequencies ($L \leq 15$ km; $T < T_f$), the KE continuum is consistent with the modal dispersion relationships of internal gravity waves (Munk 1981) (black dotted lines in Figs. 5c,d). At small spatial scales and low frequencies [$L \sim 15$ km; $T > O(1)$ day], the KE continuum quantifies the contribution of lee waves to the near-surface KE reservoir and has significant, but moderate, magnitude. IGW have the greatest energy at high frequencies ($T \leq T_f$). This suggests that near-inertial motions and the superinertial internal wave continuum make a larger contribution to the near-surface KE reservoir than low-frequency lee waves [$T > O(1)$ day].

The divergent component of IGW is less energetic overall than the rotational component across all frequencies (Figs. 5c,d). Frequency–wavenumber KE spectra are statistically more robust than our illustrative assessment of IGW in physical space at a given time step; near-inertial waves and the internal wave continuum show the largest amplitude for the rotational component, and lee waves are noticeable in both the rotational and divergent components (Figs. 4,5). This indicates that all categories of IGW—near-inertial waves, the superinertial internal wave continuum, and low-frequency lee waves—have a large rotational component and a significant divergent component.

At large spatial scales and low frequencies, the distribution of the KE of IGWs across spatiotemporal scales in our simulation might be less energetic than in other datasets. This can be explained by the forcing used in our numerical model (cf. section 1). The lack of tidal forcing results in an absence of internal tides, and the 6-h atmospheric forcing gives rise to a weaker near-inertial wave field compared to observations and numerical simulations forced with 1-h wind forcing (Song et al. 2019; Arbic et al. 2022). This suggests that our characterization of the contribution of IGWs to the winter near-surface turbulent KE cascade at submesoscale could vary in a more realistic forcing scenario. However, although we may underestimate the net contribution of IGWs to the turbulent KE cascade at the submesoscale, our characterization of the factors controlling their contributions—either to inverse or forward turbulent cascades—remains valid (cf. sections 4 and 5).

We note that the KE of IGW rotational and divergent components forms a continuum across spatiotemporal scales and does not exhibit prominent peaks at discrete inertial frequencies (Figs. 5c,d), in contrast with other datasets (Torres et al. 2018; Lahaye et al. 2019; Torres et al. 2022; Naveira Garabato et al. 2022). The dominance of an internal wave continuum over peaks of KE at discrete frequencies has also been documented in another region of highly energetic mesoscale ocean flows (Jones et al. 2023). This suggests that in such high-energy regions, the modeled IGW field is shaped by nonlinear interactions transferring KE across spatiotemporal scales, rather than by a distinct external forcing. Wave–wave, wave–eddy, and wave–mean interactions are known to scatter waves into smaller spatial scales and to transfer their KE across spatiotemporal scales (Olbers 1976; Olbers et al. 2020; Dunphy and Lamb 2014). The main KE sources for the internal wave continuum are thought to be both inertial waves and internal tides (Sugiyama et al. 2009) or primarily near-inertial waves (Le Boyer and Alford 2021). Spontaneous emission of internal gravity waves via loss of balance can also contribute to the KE continuum found at the lower end of the submesoscale range (Vanneste 2013; Alford et al. 2013; Nagai et al. 2015; Shakespeare and Hogg 2017).

The dominance of an internal wave continuum over peaks of KE at discrete frequencies supports our use of offline Lagrangian filtering to identify and isolate IGW. The internal wave continuum would not be accurately identified with methods based on the vertical structure of IGW (Torres et al. 2022), modal dispersion relationships of IGW (Torres et al. 2018; Qiu et al. 2018), or varying atmospheric forcing (Barkan et al. 2021). This is consistent with a preceding study that showed that 1) Lagrangian filtering is more accurate than other methods based on frequency–wavenumber properties at separating IGW from NWC motions in a high-energy region, while 2) the different methods lead to similar results in low-energy regions (Jones et al. 2023).

The frequency–wavenumber KE spectra have shown that the zoo of motions in the winter near-surface ocean—eddies, submesoscale fronts, near-inertial motions, lee waves, and internal wave continuum of different governing dynamics—have overlapping spatiotemporal scales, suggesting that they interact and cause turbulent KE cascades in the submesoscale range.

4. Winter turbulence across spatial scales

In this section, we characterize near-surface turbulence across spatial scales. We first use horizontal wavenumber spectra to infer the contributions of NWC and IGW motions to submesoscale turbulence. We then assess the turbulent KE cascade caused by NWC and IGW motions.

a. *Horizontal wavenumber spectra of KE*

The contributions of the rotational and divergent components of NWC and IGW motions to near-surface turbulence are inferred with horizontal wavenumber spectra of KE averaged over the 0–100-m layer (Fig. 6a). See appendix D for details of the computation of KE spectra. The total KE spectrum (plain blue line) characterizes the KE reservoir. Most of the spectral power is contained in the mesoscale

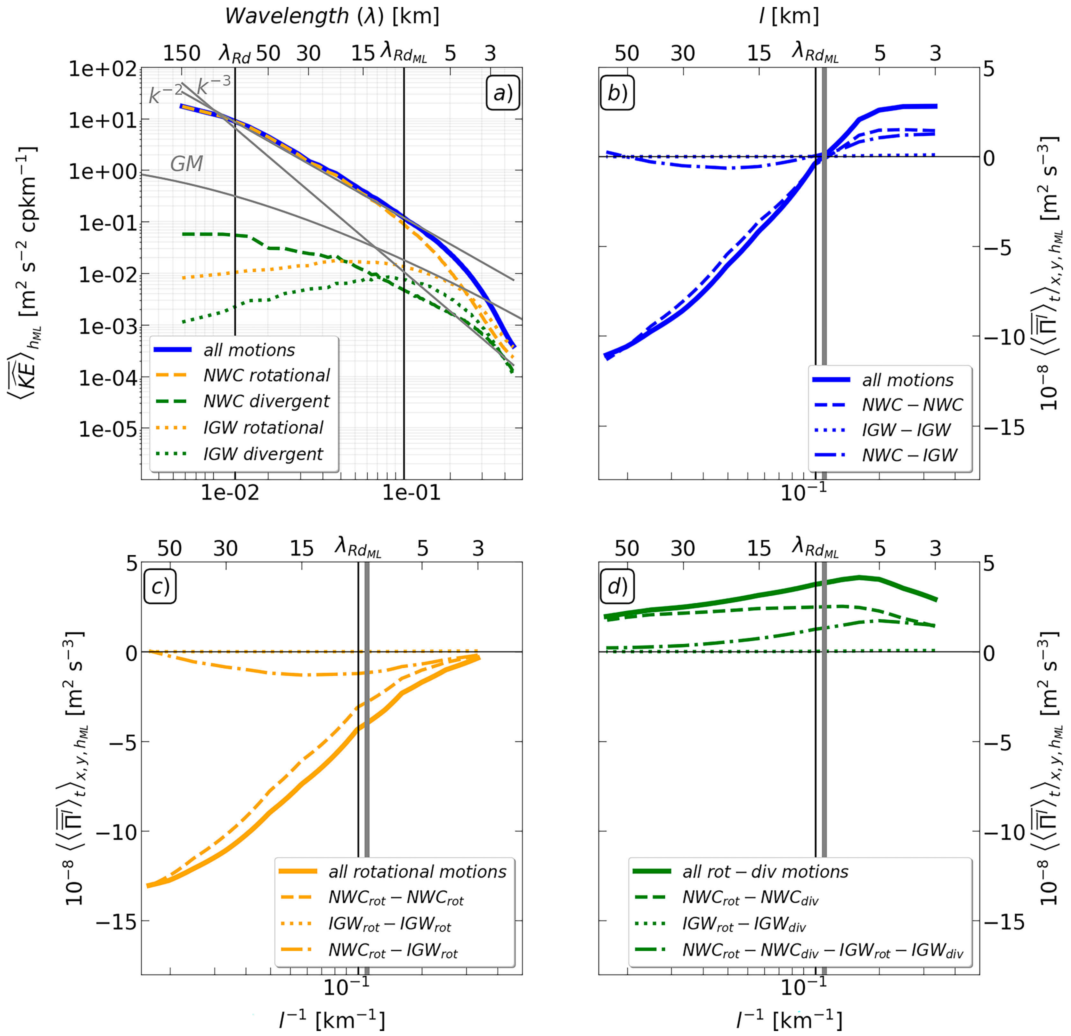

FIG. 6. Winter turbulence in the submesoscale range. (a) Temporally averaged (over 30-day simulation period) and spatially averaged (over 0–100-m layer) horizontal wavenumber KE spectra for all motions (thick blue line), NWC motions (dashed lines), and IGW motions (dotted lines) decomposed into rotational (orange) and divergent (green) components. Note that the 95% confidence limits are not shown, because they have a weak magnitude to be clearly visible (15.80% of the horizontal wavenumber KE spectra). The k^{-2}, k^{-3}, and Garrett–Munk KE spectra (Munk 1981) are plotted as references in gray. (b)–(d) Temporally and spatially averaged cross-scale KE flux for all motions (plain lines), NWC–NWC (dashed lines), IGW–IGW (dotted lines), and coupled NWC–IGW (dashed–dotted lines) interactions. Cross-scale KE flux for different classes of interactions (blue lines) in (b) are decomposed into rotational contribution (orange lines) in (c) and coupled rotational–divergent contribution (green lines) in (d). The shifting scale, from upscale (<0) to downscale (>0) cross-scale KE flux, is shown in a thick gray line.

range ($L > \lambda_{\mathrm{Rd}}$ =75 km), and decreases in the submesoscale range (λ_{Rd} =75 km $> L$) with a k^{-2} power law. This value is in line with predictions of turbulence theory (Boyd 1992; Callies and Ferrari 2013), which is associated with dual inverse and forward turbulent KE cascades in the presence of ageostrophic motions.

The total KE spectrum (plain blue line) is primarily underpinned by NWC rotational motions (dashed orange line)—eddies and submesoscale fronts—at most spatial scales. Both spectra follow similar power laws in the submesoscale range (k^{-2} and $k^{-2.3}$) and have comparable magnitudes (agreement $\geq$ 77% at $L \geq$ 10 km). The differences between the two KE spectra at the lower end of the submesoscale range are explained by IGW rotational (dotted orange line) and divergent motions (dotted green line), corresponding to near-inertial motions, lee waves, and the internal wave continuum. IGW rotational and divergent KE spectra have similar magnitudes. The spectral power increases with decreasing spatial scale and reaches a maximum at the lower end of the submesoscale range ($L \sim$ 10 km), where it 1) closely follows the Garrett–Munk KE spectrum (plain gray line) and 2) contributes significantly to the KE reservoir (~13%).

The ratio of divergent to rotational KE components [$O(0–0.2)$; not shown] increases at the lower end of the submesoscale range [$O(\geq 0.1)$ at $L \leq 9$ km; not shown], indicating an increase of the divergent component. The divergent KE component is mainly explained by NWC motions—submesoscale fronts—for $L \geq 10$ km and by IGW motions—near-inertial waves, the internal wave continuum, and lee waves—for $L \leq 10$ km. IGW divergent motions thus make a significant contribution to the KE reservoir—although of secondary importance compared to the NWC rotational motions—because they dominate the divergent KE component in the range within which the KE partitioning becomes significant.

In summary, the horizontal wavenumber KE spectra indicate that NWC rotational, IGW rotational, and IGW divergent motions, all significantly contribute to the KE reservoir and turbulent regime in the submesoscale range. The contribution of NWC rotational flows dominates at all spatial scales, whereas that of IGW motions is focused at small scales ($L < 10$ km). Next, we explicitly assess the turbulent KE cascade at the near-surface.

b. *Cross-scale kinetic energy flux*

In this subsection, we first assess the net turbulent KE cascade occurring at the near-surface, and then evaluate the individual and coupled contributions of NWC and IGW motions to the cascade. We conclude with a phenomenological description of these contributions.

1) NET CROSS-SCALE KINETIC ENERGY FLUX

(i) Spatiotemporally averaged cross-scale kinetic energy flux

The turbulent KE cascade at the near-surface is inferred from the cross-scale KE flux averaged in time and space over the 0–100-m layer (thick blue line in Fig. 6b). The cross-scale KE flux denotes an intense inverse turbulent cascade over most of the submesoscale range (negative for L in the 8–75-km range) and a weak forward turbulent cascade at the lower end of the submesoscale range (positive for $L \leq 8$ km). The inverse turbulent cascade is an order of magnitude larger than the forward cascade, and extends over a broader range of spatial scales. Thus, turbulence in the submesoscale range primarily represents a KE source for the mesoscale range in the model. The dual turbulent cascades, shown by the cross-scale KE flux, are consistent with the horizontal wavenumber spectra of KE (k^{-2} over L in the 75–5-km range; Fig. 6a) and with the wintertime turbulence documented in other oceanic regions (Sasaki et al. 2014; Schubert et al. 2019; Ajayi et al. 2021; Srinivasan et al. 2023; Naveira Garabato et al. 2022).

Inverse and forward turbulent cascades have different vertical structures across spatial scales (Fig. 7c). Negative KE fluxes are intensified through the near-surface (0–90 m) and penetrate to greater depth. The deep vertical structure of the inverse turbulent cascade is consistent with the barotropization of mesoscale eddies described by turbulent theories (Rhines 1977, 1979; Salmon 1980). Positive KE fluxes have a shallow, surface-intensified vertical structure (most intense in the 0–30-m depth range), which extends through the near-surface (0–90 m). This is consistent with the structure of fronts, identified as hotspots for the forward turbulent cascade in previous studies (Capet et al. 2008b; Schubert et al. 2020; Srinivasan et al. 2023).

(ii) Magnitude of the upscale kinetic energy flux

The inverse turbulent cascade in the Drake Passage is particularly strong [$O(10^{-7}–10^{-8})$ m^2 s^{-3}] as compared to turbulent cascades in other regions based on numerical simulations processed with similar diagnostics of the cross-scale KE flux [$O(10^{-8}–10^{-9})$ m^2 s^{-3}; Schubert et al. 2020; Srinivasan et al. 2023]. The order-of-magnitude stronger cascade in the Drake Passage could be due to either 1) a more intense near-surface submesoscale turbulence in this region or 2) the comparable, but not identical, spatiotemporal resolutions of the modeled flows between studies. Drake Passage in winter combines highly energetic mesoscale and mixed layer turbulence, which would be expected to result in a larger inverse turbulent cascade than that of other oceanic regions of intense near-surface turbulence, but low mesoscale turbulence (Capet et al. 2008a; Sasaki et al. 2014; Dong et al. 2020; Schubert et al. 2020; Naveira Garabato et al. 2022; Srinivasan et al. 2023). This hypothesis is qualitatively supported by the cross-spectrum of the vertical buoyancy flux, $\overline{w'b'}$, at 50-m depth (not shown), which shows a continuous source of KE for NWC—likely due to mixed layer baroclinic instability—across the 5–50-km range, within which the clearest intensification of the upscale KE flux is found. We will also show in section 5 that spatiotemporal resolution is an additional factor in determining the magnitude of both the inverse and forward turbulent cascades.

2) SEPARATION OF NET CROSS-SCALE KINETIC ENERGY FLUX CAUSED BY NWCS AND IGWS

(i) Spatiotemporally averaged cross-scale kinetic energy flux

NWC motions alone (dashed blue line) and NWC motions interacting with IGW motions (dashed–dotted blue line) contribute in different proportions to the two turbulent KE cascades (Fig. 6b). The inverse turbulent cascade is primarily caused by NWC–NWC interactions—eddies and submesoscale fronts—and weakly caused by NWC–IGW interactions—eddies, submesoscale fronts, near-inertial motions, lee waves, and the internal wave continuum. The forward turbulent cascade is caused by NWC–NWC and NWC–IGW interactions in roughly similar proportions. Note that IGW–IGW interactions do not cause a significant turbulent cascade [$O(10^{-10})$ m^2 s^{-3}; blue dotted line]. IGW significantly contribute to the cross-scale KE flux only through interacting with NWC motions.

The inverse turbulent cascade has been related to the absorption of submesoscale eddies by mesoscale eddies (Schubert et al. 2020), consistent with our result that interactions between eddies and submesoscale fronts (the NWC–NWC cross-scale KE flux) primarily effect an inverse turbulent cascade. The forward cascade has been related to frontogenesis (Capet et al. 2008b; Schubert et al. 2020; Srinivasan et al. 2023). This is consistent with our findings that NWC motions, including submesoscale fronts, are a main component of the forward cascade because they contribute in

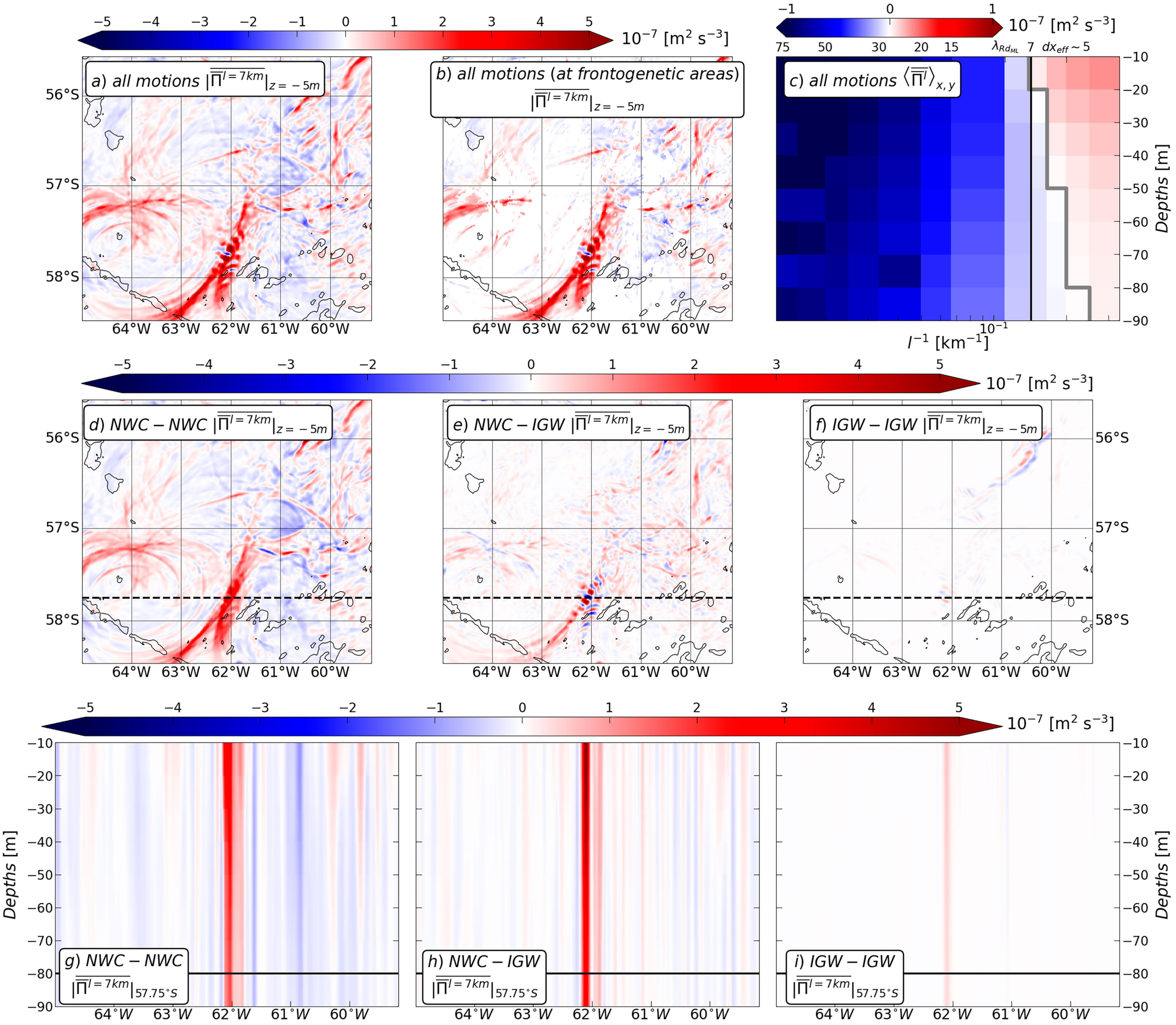

FIG. 7. Spatial structures of cross-scale KE flux. (a),(b),(d),(e),(f) Horizontal sections of temporally averaged (over 30-day simulation period) and vertically averaged (over 0–100-m layer) cross-scale KE flux at 7 km done by all motions in (a) and (b), NWC–NWC in (d), coupled NWC–IGW in (e), and IGW–IGW in (f). The field in (b) is masked to emphasize frontal areas, defined from the 10^{-15} (kg m^{-4})^2 s^{-1} contours of frontogenetic tendency [$F_s = -(\partial_x\rho\nabla_H u + \partial_y\rho\nabla_H v)\cdot\nabla_H\rho$; with (u, v) the horizontal velocities and ρ the density]. (g)–(i) Vertical sections at 57.75°S [denoted by black dotted line in (d)–(f)] of temporally averaged cross-scale KE flux at 7 km done by NWC–NWC in (g), NWC–IGW in (h), and IGW–IGW in (i). The mean mixed layer depth is shown by the black line. (c) Vertical section of temporally and horizontally averaged total cross-scale KE flux. The shifting scale, from upscale (<0) to downscale (>0) KE flux, is shown by the thick gray line. In (a), (b), and (d)–(i), the 7-km scale at which the horizontal and vertical sections of cross-scale KE flux are plotted is shown as a thin black line. All fields are plotted in the subregion shown in Fig. 2.

two forms (via the NWC–NWC and NWC–IGW cross-scale KE flux). An enhancement of the forward turbulent cascade in the presence of IGW has been documented previously (Thomas and Arun 2020; Thomas and Daniel 2021; Barkan et al. 2021). Our results accordingly show that IGW motions, including near-inertial motions, lee waves, and an internal wave continuum, enhance the forward turbulent cascade by about 43%. A recent study showed that interactions between IGWs and mesoscale eddies could result in either a KE gain or loss for mesoscale eddies (Cusack et al. 2020). This is consistent with our result that interactions between eddies, submesoscale fronts, and IGW (the NWC–IGW cross-scale KE flux) contribute to both the inverse and forward turbulent cascades.

(ii) Spatial distribution of the cross-scale kinetic energy flux

The contribution of NWC and IGW motions to the turbulent KE cascade is not uniform in space (Fig. 7). In the horizontal and vertical, the total cross-scale KE flux at 7 km corresponds to positive and negative patterns that are surface-intensified, some of which extend below the mean mixed layer base (Figs. 7a,d–i; horizontal sections of the cross-scale KE flux are shown at 7 km, where both averaged NWC and coupled NWC–IGW contributions are positive and of comparable magnitude). The bulk of the positive total KE flux (forward turbulent KE cascade) is found in areas of positive frontogenetic tendency (fronts defined as $F_s > 10^{-15}$ (kg m^{-4})^2 s^{-1}; Fig. 7b). The cross-scale KE flux spatially averaged over frontal areas (3×10^{-8} m^2 s^{-3}) is positive and larger by about a factor of 4.5 than the domain average (6.5×10^{-9} m^2 s^{-3}). This points to fronts as key foci of the submesoscale forward cascade, occurring in the presence or absence of waves.

The total cross-scale KE flux results from the combination of NWC–NWC and NWC–IGW cross-scale KE flux, which have signs that either locally cancel or accumulate (Figs. 7d–i). The NWC–NWC cross-scale KE flux corresponds to elongated, smooth horizontal patterns, consistent with submesoscale fronts [section 3a(1)], and of fairly uniform magnitude across the domain. The NWC–IGW cross-scale KE flux corresponds to small-scale patterns, denoting the imprint of internal gravity waves [section 3a(2)]. These patterns show no coherent structure and have heterogeneous magnitudes, with areas either of lower or larger magnitude than the NWC–NWC contribution. The IGW–IGW cross-scale KE flux is of lower magnitude, as already shown from the temporally and spatially averaged KE flux (Fig. 6b). It locally contributes to the positive cross-scale KE flux at about 62°W (Figs. 7f,i), but does not significantly contribute to the total term overall (Fig. 6b).

In summary, NWC and IGW motions contribute to the inverse and forward turbulent cascades. This indicates that the direction of the turbulent cascade is driven by a factor other than the category of oceanic motions (NWC or IGW). To separate the two turbulent cascades, we further decompose NWC–NWC and coupled NWC–IGW cross-scale KE flux into dynamical components in the next section.

3) SEPARATION OF UP/DOWN-SCALE KINETIC ENERGY FLUX CAUSED BY NWCS AND IGWS

(i) Spatiotemporally averaged cross-scale kinetic energy flux

The decomposition of NWC and coupled NWC–IGW cross-scale KE flux into dynamical components enables us to separate the inverse and forward turbulent cascades (Figs. 6c,d). The cross-scale KE flux for the different dynamical components [all rotational motions, $\mathrm{NWC_{rot}}$–$\mathrm{NWC_{rot}}$, and $\mathrm{NWC_{rot}}$–$\mathrm{IGW_{rot}}$ in Fig. 6c; all rotational–divergent (rot–div) motions, $\mathrm{NWC_{rot}}$–$\mathrm{NWC_{div}}$, and $\mathrm{NWC_{rot}}$–$\mathrm{NWC_{div}}$–$\mathrm{IGW_{rot}}$–$\mathrm{IGW_{div}}$ in Fig. 6d] do not change sign across spatial scales, such that each component exclusively performs one turbulent cascade. The net NWC–NWC and NWC–IGW cross-scale KE flux (Fig. 6b) change sign, where a change of balance occurs between the cross-scale KE flux of the different dynamical components (Figs. 6c,d).

The inverse turbulent cascade (plain orange line) is mainly caused by $\mathrm{NWC_{rot}}$–$\mathrm{NWC_{rot}}$ interactions (dashed orange line)—eddies and the rotational component of fronts—and more weakly by $\mathrm{NWC_{rot}}$–$\mathrm{IGW_{rot}}$ interactions (dashed–dotted orange line)—eddies, rotational component of fronts, near-inertial motions, lee waves, and the internal wave continuum (Fig. 6c). The forward turbulent cascade (plain green line) is achieved in roughly similar proportions by $\mathrm{NWC_{rot}}$–$\mathrm{NWC_{div}}$ interactions (dashed green line)—eddies and both components of fronts—and by $\mathrm{NWC_{rot}}$–$\mathrm{NWC_{div}}$–$\mathrm{IGW_{rot}}$–$\mathrm{IGW_{div}}$ interactions (dashed–dotted line)—eddies and both components of fronts interacting with near-inertial motions and both components of lee waves and the internal wave continuum (Fig. 6d). Note that purely $\mathrm{NWC_{div}}$–$\mathrm{NWC_{div}}$ and $\mathrm{NWC_{div}}$–$\mathrm{IGW_{div}}$ interactions do not significantly contribute to the turbulent cascades [$O(10^{-9})$ m^2 s^{-3}; not shown].

The decomposition of the cross-scale KE flux into dynamical components refines our understanding of the turbulent KE cascades (Capet et al. 2008b; Molemaker et al. 2010; Callies and Ferrari 2013). The forward cascade is not due to divergent motions alone, but occurs when divergent and rotational motions are coupled. Rotational motions are therefore as important as divergent motions for the forward turbulent cascade, in agreement with a recent study by Srinivasan et al. (2023).

(ii) Role of flow partitioning into rotational and divergent components

The governing dynamics of motions (rotational versus coupled rotational–divergent) explain the direction of the turbulent cascade. The contributions of NWC and coupled NWC–IGW motions to the turbulent cascade are therefore underpinned by their partitioning into dynamical components. The partitioning of NWC motions into dynamical components indicates that they are largely rotational [$\widehat{\mathrm{KE}}_{\mathrm{div}}/\widehat{\mathrm{KE}}_{\mathrm{rot}}$ about $O(0–0.15)$; Fig. 6a]. This causes the NWC-induced upscale KE flux ($\mathrm{NWC_{rot}}$–$\mathrm{NWC_{rot}}$ cross-scale KE flux: dashed orange line) to overcome the NWC-induced downscale KE flux ($\mathrm{NWC_{rot}}$–$\mathrm{NWC_{div}}$ cross-scale KE flux: dashed green line) over most spatial scales (Figs. 6b–d). The NWC-induced downscale KE flux ($\mathrm{NWC_{rot}}$–$\mathrm{NWC_{div}}$ cross-scale KE flux: dashed green line) has a relatively constant magnitude across all spatial scales, but it dominates the NWC-induced net turbulent cascade (NWC–NWC cross-scale KE flux: dashed blue line) at $L < 8$ km, where the partitioning of NWC into dynamical components indicates an increase of the divergent component ($\widehat{\mathrm{KE}}_{\mathrm{div}}/\widehat{\mathrm{KE}}_{\mathrm{rot}} > 0.1$ at $L < 10$ km; not shown).

The IGW motions are close to being equipartitioned between rotational and divergent components [$\widehat{\mathrm{KE}}_{\mathrm{div}}/\widehat{\mathrm{KE}}_{\mathrm{rot}}$ in $O(0.1–0.5)$; Fig. 6a]. This results in an NWC–IGW upscale KE flux ($\mathrm{NWC_{rot}}$–$\mathrm{IGW_{rot}}$ cross-scale KE flux: dashed–dotted orange line) and an NWC–IGW downscale KE flux ($\mathrm{NWC_{rot}}$–$\mathrm{NWC_{div}}$–$\mathrm{IGW_{rot}}$–$\mathrm{IGW_{div}}$ cross-scale KE flux: dashed–dotted green line) of similar magnitudes, in contrast with the NWC KE flux (dashed orange and green lines; Figs. 6b–d).

Wintertime near-surface turbulence is heterogeneous across spatial scales (Figs. 6a–d). One class of motions—NWC rotational motions, i.e., eddies and the rotational component of submesoscale fronts—drives a large inverse turbulent cascade, which dominates across most spatial scales ($L > 8$ km). Interactions between all classes of motions—NWC rotational and divergent motions, i.e., eddies, submesoscale fronts, and IGW rotational and divergent motions, i.e., near-inertial motions, lee waves, and the internal wave continuum—cause a forward turbulent cascade, which dominates at the lower end

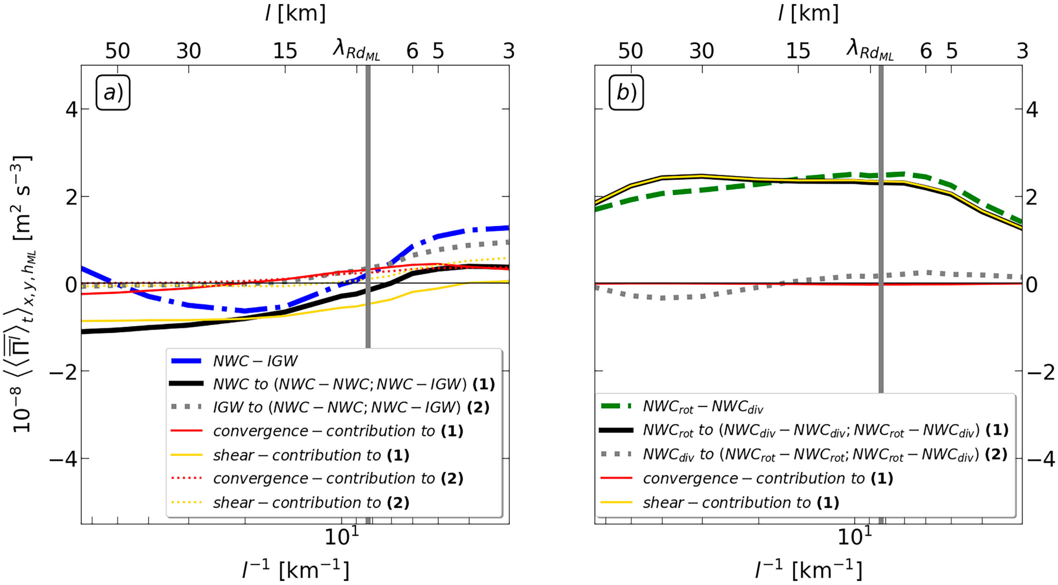

FIG. 8. Cross-scale KE flux caused by NWC–IGW and $\mathrm{NWC}_{\mathrm{rot}}$–$\mathrm{NWC}_{\mathrm{div}}$ interactions. (a),(b) Temporally and spatially averaged (over 30-day simulation period and 0–100-m layer) cross-scale KE flux for NWC–IGW motions in (a) and $\mathrm{NWC}_{\mathrm{rot}}$–$\mathrm{NWC}_{\mathrm{div}}$ motions in (b). Cross-scale KE fluxes are decomposed into the two types of coupling shown in Eq. (4) (dotted gray lines and plain black lines) and into convergence and strain contributions shown in Eq. (3) (red and yellow lines). The shifting scale, from upscale (<0) to downscale (>0) cross-scale KE flux, is shown in a thick gray line.

of the submesoscale range ($L < 8$ km). In the following, we further our understanding of NWC–IGW and $\mathrm{NWC}_{\mathrm{rot}}$–$\mathrm{NWC}_{\mathrm{div}}$ interactions leading to a forward turbulent cascade.

4) Downscale kinetic energy flux caused by NWC–IGW and NWCrot–NWCdiv interactions

Here, we evaluate the specific combinations of motions, involved in NWC–IGW and $\mathrm{NWC}_{\mathrm{rot}}$–$\mathrm{NWC}_{\mathrm{div}}$ interactions, that lead to a downscale KE flux. We first document the KE flux across the different motions—meaning which motion is either dampened or energized—by decomposing the coupled cross-scale KE flux into different types of coupling [Eq. (4)]. We then evaluate the mechanism of the downscale KE flux by attributing it to convergent or straining processes [Eq. (3); Polzin (2010), Cusack et al. (2020), Srinivasan et al. (2023), Freilich et al. (2023)].

(i) NWC–IGW interactions

The NWC–IGW downscale KE flux (blue dashed–dotted line; Fig. 8a) takes the form of 1) a coupling between the gradient of low-pass filtered IGW velocities and high-pass filtered NWC–NWC and NWC–IGW stresses (gray dotted line; 69% of the NWC–IGW downscale KE flux), and 2) a coupling between the gradient of low-pass filtered NWC velocities and high-pass filtered NWC–NWC and NWC–IGW stresses (black plain line; 31% of the NWC–IGW downscale KE flux). These results indicate that the NWC–IGW downscale KE flux primarily corresponds to a KE transfer 1) from large-scale IGW motions to small-scale NWC and IGW motions, and 2) from large-scale NWC motions to small-scale NWC and IGW motions. Our result shows that IGW can energize NWC in the submesoscale range via a forward turbulent cascade. This key finding is the counterpart of the previously described KE transfer from IGW to NWC in the mesoscale range, via an inverse turbulent cascade (Cusack et al. 2020).

The subsequent decomposition of cross-scale KE flux into convergence and horizontal strain contributions [Eq. (3)] shows that 1) the IGW to NWC–IGW downscale KE flux is roughly evenly convergence- and strain-driven (43% and 57%; red and yellow dotted lines in Fig. 8a), and 2) the NWC to NWC–IGW downscale KE flux is primarily convergence-driven (red plain line in Fig. 8a). The result that convergence is the main mechanism channeling KE of NWC and IGW downscale is another element pointing toward fronts (oceanic features of large convergence) as hotspots of NWC and IGW interactions. This is also important for our understanding of internal wave energetics. Divergence is usually assumed to play a negligible role in channeling KE between internal waves and nonwave currents, with strain considered as the only substantial factor (Polzin 2010; Cusack et al. 2020). The result that strain is a significant mechanism transferring KE of IGW downscale indicates that straining of IGW can facilitate energy transfers to submesoscale NWC.

For reasons of computational cost, we did not explicitly decompose the contributions of $\mathrm{IGW}_{\mathrm{rot}}$, $\mathrm{IGW}_{\mathrm{div}}$, $\mathrm{NWC}_{\mathrm{rot}}$, and $\mathrm{NWC}_{\mathrm{div}}$ to the NWC–IGW downscale KE flux, which represents 16 different couplings. However, we suggest that all components may be important, since $\mathrm{IGW}_{\mathrm{div}}$ and $\mathrm{NWC}_{\mathrm{div}}$ should dominate the leading-order convergence-driven NWC–IGW downscale

KE flux, and $\mathrm{IGW}_{\mathrm{rot}}$ could be of significance via the strain-driven NWC–IGW downscale KE flux.

(ii) $\mathrm{NWC}_{\mathrm{rot}}$–$\mathrm{NWC}_{\mathrm{div}}$ interactions

The $\mathrm{NWC}_{\mathrm{rot}}$–$\mathrm{NWC}_{\mathrm{div}}$ downscale KE flux (green dashed line; Fig. 8b) takes the form of a coupling between the gradient of low-pass filtered $\mathrm{NWC}_{\mathrm{rot}}$ velocities and high-pass filtered $\mathrm{NWC}_{\mathrm{rot}}$–$\mathrm{NWC}_{\mathrm{div}}$ and $\mathrm{NWC}_{\mathrm{div}}$–$\mathrm{NWC}_{\mathrm{div}}$ stresses (black plain line; 89% of the $\mathrm{NWC}_{\mathrm{rot}}$–$\mathrm{NWC}_{\mathrm{div}}$ downscale KE flux). This indicates that the $\mathrm{NWC}_{\mathrm{rot}}$–$\mathrm{NWC}_{\mathrm{div}}$ downscale KE flux primarily corresponds to a KE transfer from large-scale $\mathrm{NWC}_{\mathrm{rot}}$ motions to small-scale $\mathrm{NWC}_{\mathrm{rot}}$ and $\mathrm{IGW}_{\mathrm{div}}$ motions.

The subsequent decomposition of cross-scale KE flux into convergence and horizontal strain [Eq. (3)] reveals that the $\mathrm{NWC}_{\mathrm{rot}}$ to $\mathrm{NWC}_{\mathrm{div}}$ downscale KE flux is exclusively strain-driven (yellow plain line in Fig. 8b). This indicates that the straining of $\mathrm{NWC}_{\mathrm{rot}}$ facilitates energy transfer to $\mathrm{NWC}_{\mathrm{div}}$ and $\mathrm{NWC}_{\mathrm{rot}}$. This is only partially consistent with Srinivasan et al. (2023), who predicted and showed the equipartitioning of downscale KE transfers caused by NWC motions between convergent and strain components, using asymptotic theory and a numerical simulation. However, it is fully consistent with Freilich et al. (2023), who indicated the predominance of shear strain at a front, associated with the total flow (NWC plus IGW), within an observational snapshot.

Our characterization of winter submesoscale turbulence shows that all classes of motions are required in order to comprehensively capture the effects of the turbulence (i.e., the inverse and forward turbulent KE cascades). This has direct implications for the spatiotemporal resolution of motions needed to infer the forward turbulent cascade occurring at small scales. Spatiotemporal resolution considerations may also be of importance for the inverse turbulent cascade, which is mainly caused by NWC rotational motions that extend to small scales ($L \geq 1$ km; $T \geq 2$ h in Fig. 5).

5. Sensitivity of winter turbulence to spatiotemporal resolution of flow

In this section, we characterize the sensitivity of winter near-surface turbulence occurring at the submesoscale to the spatiotemporal resolution of motions. The winter turbulence characterized in the previous sections represents our model benchmark. Our model solves ocean dynamics down to 1 km, with an effective resolution of about 5 km [cf. section 2a(1)]. At these spatial scales, the smallest period of flows resolved in our model is hourly. This is based on the convergence between horizontal wavenumber spectra of KE and cross-scale KE flux inferred from hourly averages and snapshots [agreement of $O(>75\%)$; Fig. 9]. We therefore consider combinations of spatiotemporal resolutions coarser than 1 km and 1 h (referred to below as "measurement resolutions"), that we classify, first, into coarser submesoscale scenarios and, then, mesoscale-only scenarios. For simplicity, we consider the total winter turbulence—inferred from the nonseparated (NWC plus IGW) total (rotational plus divergent) modeled velocities—and refer to the previous sections to interpret the results in terms of classes of motion.

We analyze coarser spatiotemporal scenarios of winter near-surface turbulence using horizontal wavenumber spectra of KE and cross-scale KE flux inferred from model outputs that were coarsened using offline temporal and spatial filtering (Figs. 9a,b). The analysis of coarser scenarios against the model benchmark requires the definition of an effective resolution for coarser spatial, temporal, and spatiotemporal scales. The effective resolution measures the numerical dissipation range and is usually defined by the wavelength below which the wavenumber KE spectrum sharply decreases, departing from the submesoscale turbulent regime (k^{-2}; Skamarock 2004; Soufflet et al. 2016; Callies and Ferrari 2013). However, this definition is not adequate for the temporally coarse scenarios, which at all scales show smoother spectral slopes than the spatially coarse scenarios. In the spatially coarse scenarios, the effective resolution corresponds to a 20% magnitude difference between the model's benchmark (plain blue line) and coarse wavenumber KE spectra (other-color lines; Fig. 9). We use this alternative definition—based on a decrease of KE magnitude—to infer an effective resolution in the temporally coarsened scenarios. In addition, we infer the underestimation of the inverse turbulent cascade in coarser scenarios by comparing the coarser cross-scale KE flux accumulated in the 50–8-km range to the model's benchmark.

a. Coarser submesoscale scenarios

We first characterize the sensitivity of the winter near-surface turbulence to coarser submesoscale scenarios (hourly/$dx \sim 5$ km, hourly/$dx \sim 10$ km, 6-hourly/$dx \sim 1, 5$ km; Fig. 9a,b).

1) HOURLY/$DX \sim 5$ KM

The $dx \sim 5$ km horizontal measurement resolution, corresponding to a 15-km effective resolution (Fig. 9a), mostly impacts IGW. It filters out and underestimates a significant part of IGW rotational and divergent motions—the internal wave continuum—and of NWC rotational motions—submesoscale eddies and fronts—(Fig. 5). This results in a slightly weaker KE partitioning into rotational and divergent components at small scales ($\widehat{\mathrm{KE}_{\mathrm{div}}}/\widehat{\mathrm{KE}_{\mathrm{rot}}} < 0.15$ at $L < 10$ km; not shown) than for the model's benchmark ($\widehat{\mathrm{KE}_{\mathrm{div}}}/\widehat{\mathrm{KE}_{\mathrm{rot}}} < 0.25$ at $L < 10$ km; not shown), because IGW motions explain most of the divergent KE over this spatial range.

The characteristics of the $dx \sim 5$ km horizontal wavenumber spectra of KE ($k^{-2.1}$ power law in the 75–15-km range and an underestimation of divergent KE component at $L < 10$ km; Fig. 9a) suggest a turbulent regime consistent with submesoscale turbulence, but a weaker forward turbulent cascade. This is confirmed by the cross-scale KE flux (Figs. 9b and 10). The $dx \sim 5$ km resolution allows inference of a reasonably good estimate of the inverse turbulent cascade (underestimation of 16% in the 50–8-km range compared to the model's benchmark), but does not permit an inference of a reliable forward turbulent cascade (weak downscale KE flux at $L < 8$ km, below the effective resolution at $L \sim 15$ km).

The $dx \sim 5$ km winter turbulence emphasizes the critical role of NWC motions (submesoscale eddies and rotational fronts) and IGW motions (the internal wave continuum) of

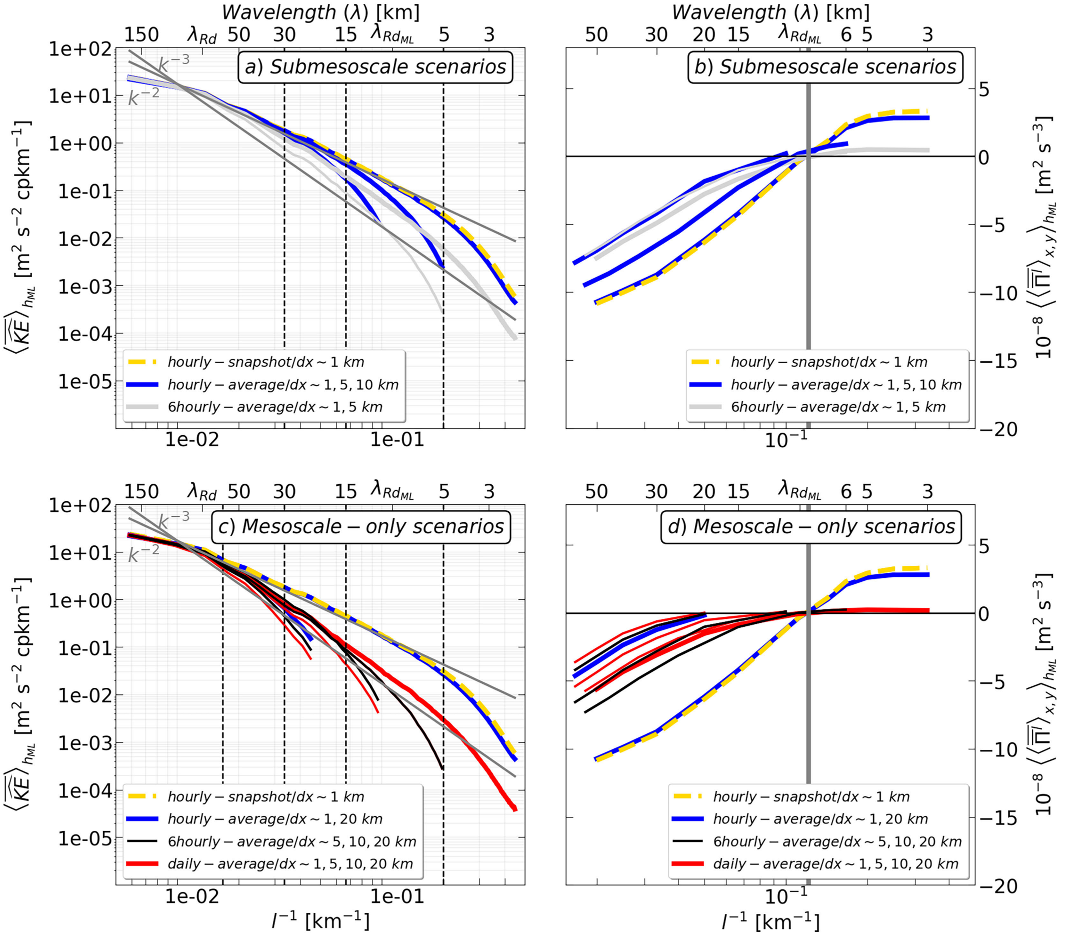

FIG. 9. Sensitivity of winter submesoscale turbulence to spatiotemporal resolutions. Temporally averaged (over 30-day simulation period) and spatially averaged (over 0–100-m layer) (a),(c) horizontal wavenumber KE spectra and (b),(d) cross-scale KE flux, for different horizontal resolutions ($dx \sim 1$, 5, 10, 20 km; different line lengths) and temporal resolutions (hourly, 6-hourly, and daily averages; different line colors). The model's benchmark [dotted yellow lines in (a)–(d)] corresponds to hourly/$dx \sim 1$ km resolutions. (top) Coarser submesoscale scenarios are shown (hourly/$dx \sim 5$, 10 km and 6-hourly/$dx \sim 1$ km, 5 km resolutions). (bottom) Mesoscale-only scenarios (hourly/$dx \sim 20$ km, daily/$dx \sim 1$ km resolutions and combinations of 6-hourly, daily averages and horizontal $dx \sim 5$, 10, and 20 km resolutions) are shown. In (a) and (c), k^{-2}, k^{-3} power laws are plotted as references in gray and the different effective resolutions are marked by vertical dotted black lines. In (b) and (d), the shifting scale, from upscale (<0) to downscale (>0), is shown in the thick gray line.

small spatial scales ($L < 15$ km) in the forward turbulent cascade. This indicates that 1) IGW motions mainly contribute to the forward cascade as an internal wave continuum in our model, and 2) NWC rotational motions may also be important for the forward turbulent cascade.

2) HOURLY/$DX \sim 10$ KM, 6-HOURLY/$DX \sim 1$ KM, AND 6-HOURLY/$DX \sim 5$ KM

The $dx \sim 10$ km and 6-hourly temporal measurement resolutions (corresponding to a 30-km effective resolution; Fig. 8a) correspond to scenarios mainly entailing NWC flows. They have in common that they filter out and underestimate the most energetic part of IGW rotational and divergent motions (the internal wave continuum), a significant part of NWC rotational flows (submesoscale eddies and fronts) and a fraction of NWC divergent motions such as submesoscale fronts (Fig. 5). The 6-hourly measurement resolution results in a significantly larger KE partitioning ($\widehat{\mathrm{KE}}_{\mathrm{div}}/\widehat{\mathrm{KE}}_{\mathrm{rot}} < 0.40$ at $L < 5$ km; not shown) than that of the model's benchmark ($\widehat{\mathrm{KE}}_{\mathrm{div}}/\widehat{\mathrm{KE}}_{\mathrm{rot}} < 0.25$ at $L < 5$ km), indicating that the coarser temporal resolution preferentially leads to rotational motions.

Coarse wavenumber KE spectra follow steeper power laws than k^{-2} in the 75–30-km range (Fig. 9a), suggesting turbulent regimes at the transition between submesoscale turbulence (k^{-2}; Callies and Ferrari 2013) and quasigeostrophic turbulence (k^{-3}; Charney 1971). This is confirmed by the coarse cross-scale KE flux (Figs. 9b and 10). Coarser submesoscale resolutions ($L > 10$ km; $T > 6$ h) than used by the model ($L \sim 1$ km; $T = 1$ h) result in an underestimated inverse turbulent cascade (underestimation of 28%–30%; Figs. 9b and 10),

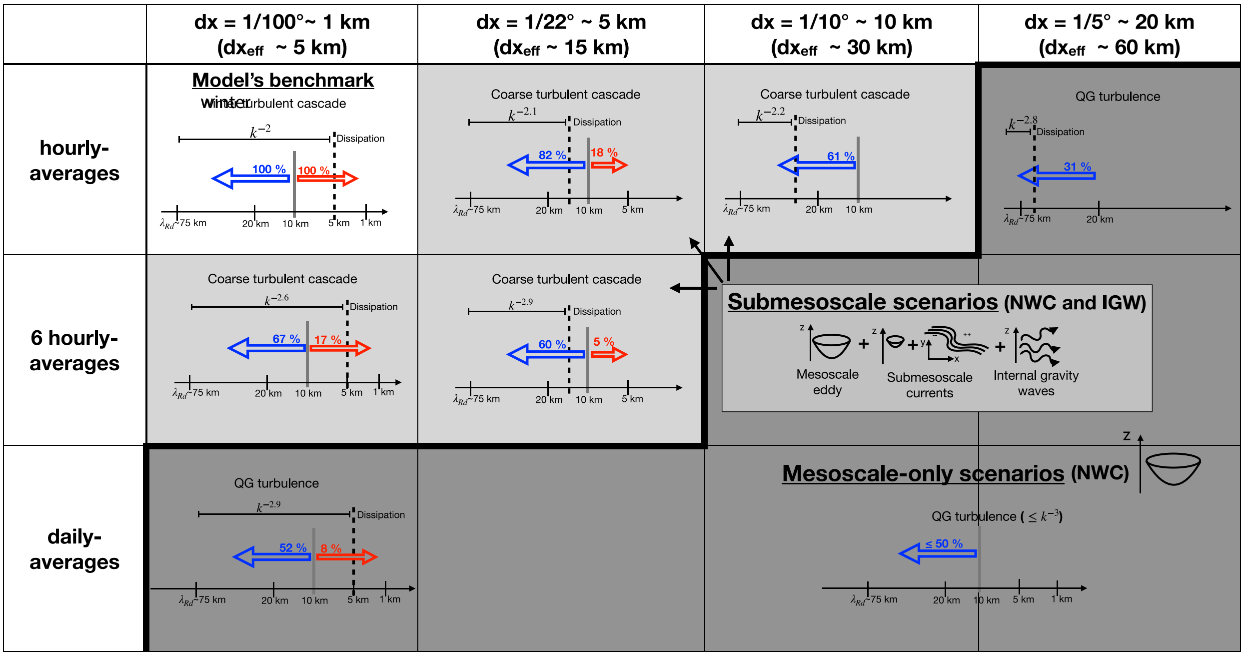

FIG. 10. Schematic of winter submesoscale turbulent regimes according to spatiotemporal measurement resolutions. Turbulent regimes are classified in three categories: model's benchmark (hourly/$dx \sim 1$ km in white), submesoscale scenarios (hourly/$dx \sim 5$ km; hourly/$dx \sim 10$ km; 6-hourly/$dx \sim 1$, 5 km; in slight gray) and mesoscale-only scenarios (hourly/$dx \sim 20$ km; daily/$dx \sim 1$ km and others in dark gray). A schematic of NWC and IGW motions: mesoscale eddies, submesoscale eddies, submesoscale fronts (all in NWC) and IGWs are shown in order. Turbulence is assessed from the spectral slope (k^{-x}; with x the power law), and the magnitude of inverse (blue arrows) and forward turbulent cascades (red arrows) is compared to the model's benchmark (%). Effective horizontal resolutions are marked by dotted black lines and shifting scale—from inverse to forward cascade—with gray lines.

and a near-vanishing forward turbulent cascade (6-hourly/$dx \sim 1$, 5 km: underestimation of 80%–95%; or hourly/$dx \sim 10$ km: resolution coarser than the spatial range of the downscale KE flux, at $L \leq 8$ km; Figs. 9b and 10).

The substantially modified winter turbulence for coarser submesoscale scenarios highlights the key role of NWC and IGW rotational motions of small spatiotemporal scales (10 km $\geq L \geq$ 1 km and 6 h $\geq T \geq$ 2 h) in, both, the forward (80%–95%) and inverse (up to 30%) turbulent cascades. These results confirm that rotational motions are as important for the forward turbulent cascade as for the inverse cascade. Small spatiotemporal scales primarily contain rotational motions, such that the limiting factor is thereby not the resolution of the divergent component of motions (fronts and internal wave continuum), but the resolution of NWC and IGW rotational motions—eddies, fronts, and the internal wave continuum—(Fig. 5). Spatiotemporal scales therefore appear to pose the critical criterion for the occurrence of a forward turbulent cascade; and the criterion of governing dynamics—involving the increasing partitioning of KE into the divergent component—plays a weaker role [cf. section 4b(3)].

The significant sensitivity of the forward and inverse turbulent cascades to the spatiotemporal resolution of motions also indicates that the different classes of motions play dynamical roles of distinct importance. IGW motions are a major contributor to the forward turbulent cascade in the form of the superinertial internal wave continuum ($T < T_f$). This implies that superinertial IGW contribute more to submesoscale turbulence than near-inertial motions and low-frequency lee waves. We may then conclude that bottom-generated lee waves, which are quasi-stationary by definition, do not make a leading-order contribution to submesoscale turbulence at the near-surface, as previously suggested by the results of 1) lee waves accounting for a large fraction of rotational and divergent KE at small spatial scales ($L < 15$ km) and 2) the forward turbulent cascade at small spatial scales being caused by coupled rotational–divergent motions (Figs. 4 and 6).

A comprehensive understanding of the contributions of different classes of flows to near-surface turbulence is thus contingent on the motions' governing dynamics [section 4b(3)] along with their spatiotemporal scales.

b. *Mesoscale-only scenarios*

Here we present in detail the winter near-surface turbulence for the hourly/$dx \sim 20$ km and daily/$dx \sim 1$ km cases, which capture the upper bounds of the mesoscale range [$L <$ Rd $\sim$ 75 km; $L < O$(days)] and are representative of all mesoscale-only scenarios (hourly/$dx \sim 20$ km; 6-hourly/$dx \sim 10$, 20 km; and daily/$dx \sim 1$, 5, 10, and 20 km; Fig. 10). The $dx \sim 20$ km and daily measurement resolutions (corresponding to a 60-km effective resolution; Fig. 9c) drastically impact all classes of motion, with the exception of NWC rotational motions. These scenarios filter out and largely underestimate all classes of motion in the submesoscale range—IGW motions, i.e., near-inertial motions, lee waves, and the internal wave continuum, and NWC motions, i.e., eddies and fronts (Fig. 5). NWC rotational motions in the mesoscale range and the upper end of the submesoscale range are adequately reproduced ($L > 20$ km; $T > 1$ day).

Coarse horizontal wavenumber spectra of KE follow power laws equal to or steeper than k^{-3} in the 75–60-km spatial range (Fig. 9c), suggesting turbulent regimes close to quasi-geostrophic turbulence (Charney 1971). This is confirmed by the cross-scale KE flux, which exhibits an inverse turbulent cascade underestimated by ≥50% compared to the model benchmark (Figs. 9d and 10).

The coarser submesoscale and mesoscale-only scenarios emphasize the large contribution of the submesoscale range to the inverse turbulent cascade (Figs. 9b,d and 10). The full submesoscale range ($L_{\mathrm{eff}} \leq 60$ km; 1 day $\geq T \geq 2$ h) and the lower end of the submesoscale range ($L_{\mathrm{eff}} \leq 30$ km; 6 h $\geq T \geq 2$ h, with L_{eff} the effective resolution) respectively account for about 50% and 30% of the inverse turbulent cascade (Fig. 10). In a forthcoming study, we will investigate the role of submesoscale currents as a potentially significant KE source for the mesoscale eddy field in the Southern Ocean.

6. Summary and discussion

In this study, we have investigated the physics governing the spatiotemporal scales of near-surface submesoscale turbulence in the Drake Passage in winter. We first assessed the contributions of nonwave currents (NWCs) and internal gravity waves (IGWs) to submesoscale turbulence, after which we characterized their energetic contributions in terms of governing dynamics—i.e., partitioning into rotational and divergent components—and spatiotemporal scales. Our analysis used an observationally verified high-resolution regional numerical simulation, combined with an offline Lagrangian filter and a Helmholtz decomposition to 1) separate the modeled flow into classes of motions (NWC versus IGW) and 2) assess their governing dynamics (rotational versus divergent). Our main findings are summarized and their implications explored in this section.

a. Contributions of NWC and IGW motions to the winter submesoscale turbulence

In the region of the Drake Passage, the winter submesoscale turbulence supports an inverse turbulent KE cascade at the near-surface, over most spatial scales ($\lambda_{\mathrm{Rd}} = 75 > L > 8$ km), and a weak forward cascade, below 8 km (Figs. 6b and 7). The submesoscale turbulence, therefore, mainly represents a KE source for the mesoscale range ($L > \lambda_{\mathrm{Rd}} = 75$ km) in this region in wintertime. This is consistent with the seasonality of mesoscale eddies—being the most intense in spring due to an inverse submesoscale turbulent cascade in winter—documented in other oceanic regions (Qiu et al. 2014; Sasaki et al. 2014; Uchida et al. 2017; Dong et al. 2020; Schubert et al. 2020).

Our analysis shows that both NWC and IGW motions contribute to the inverse and forward turbulent KE cascades in the submesoscale range (Figs. 6b and 7d,e,g,h). NWC motions are responsible for most of the inverse turbulent cascade (94%) and a significant fraction of the forward one (54%). This is consistent with the views of submesoscale eddies causing an intense inverse turbulent cascade (Klein et al. 2019; Schubert et al. 2020; Srinivasan et al. 2023) and substantially energizing mesoscale eddies. IGW contribute significantly to the forward turbulent cascade (43%) when coupled to NWC motions. This is consistent with the view of internal gravity waves acting mainly to enhance the forward cascade (Polzin 2010; Whitt and Thomas 2015; Barkan et al. 2017; Rocha et al. 2018; Thomas and Arun 2020; Thomas and Daniel 2021; Barkan et al. 2021). One of our key findings is that the NWC–IGW forward cascade is primarily caused by a transfer from large-scale IGW to small-scale NWC and IGW motions (Fig. 8a). This result indicates that IGW can enhance the forward cascade by energizing NWC and IGW motions in the submesoscale range, in addition to the previously documented processes of mesoscale eddy dampening (Barkan et al. 2021).

Our analysis provides evidence that the contributions of NWC and IGW motions to winter submesoscale turbulence are driven by 1) their governing dynamics (partitioning into rotational and divergent components) and 2) their spatiotemporal characteristics (Figs. 6c,d, 9, and 10). We have shown that the governing dynamics set the direction of the turbulent KE cascade, consistent with a recent modeling study (Srinivasan et al. 2023). The inverse turbulent cascade is caused by the purely rotational component of NWC and coupled NWC–IGW motions, and the forward turbulent cascade is caused by interactions between rotational and divergent components of NWCs and coupled NWC–IGW motions (Figs. 6c,d). The NWC–NWC forward cascade is mainly caused by a transfer from large-scale $\mathrm{NWC}_{\mathrm{rot}}$ to small-scale $\mathrm{NWC}_{\mathrm{rot}}$ and $\mathrm{NWC}_{\mathrm{div}}$ motions (Fig. 8b). Our analysis has also shown that the governing dynamics of motion are a necessary, but not sufficient factor to explain the contribution of NWC and IGW motions to the turbulent KE cascade. Coarsening of the spatiotemporal resolution of NWC and IGW motions decreases the magnitude of the two turbulent cascades. Small spatiotemporal scales ($L < 10$ km; $T < 6$ h) 1) are mainly rotational (Fig. 5) and 2) account respectively for most of (80%–95%) the forward cascade and a significant fraction (30%) of the inverse cascade of turbulent KE (Figs. 9 and 10).

Our study gives a comprehensive and nuanced view of near-surface submesoscale turbulence in the Drake Passage in wintertime. We note that our quantification of the contributions of NWC and IGW to the turbulent KE cascade at the submesoscale may be sensitive to our specific choice of region, season of study, and model [cf. sections 2a(2) and 3b(2)]. However, we argue that our characterization of the factors controlling their contribution remains valid overall. The inverse turbulent cascade is caused by interactions between rotational submesoscale eddies and the rotational component of fronts, of which small spatiotemporal scales ($L < 10$ km; $T < 6$ h) represent a significant fraction. The forward turbulent cascade is caused by interactions between motions of small spatiotemporal scales ($L < 10$ km; $T < 6$ h), which are significantly rotational and correspond to an internal wave continuum, as well as submesoscale eddies and fronts. Although lee waves represent a significant component of the near-surface KE reservoir at small scales in our model

($L < 15$ km), our analysis suggests that they are not a significant contributor to the forward turbulent cascade due to their low frequency [$T > O(\text{day})$].

b. *Implications for observations and modeling*

Our assessment of the sensitivity of winter submesoscale turbulence to spatiotemporal resolution points to several important implications for our dynamical understanding of turbulent KE cascades and for the observational and modeling strategies adopted to study it. We must note, however, that our analysis is not exhaustive from a real-world perspective, because smaller scales not captured by our model ($L < 1$ km; $T < 1$ h) may impact the magnitude and energy transfer properties of winter turbulence.

We have shown that the winter turbulent KE cascade is strongly sensitive to spatiotemporal measurement resolution. This indicates that all classes of flows should be resolved or measured at higher spatiotemporal resolution ($L < 10$ km; $T < 6$ h) than those considered in most regional studies to diagnose winter turbulence comprehensively. This raises questions about the comparability of regional studies (earlier and ours) of submesoscale turbulence that were based on models with different spatiotemporal resolutions, and therefore highlights gaps in our general understanding of near-surface submesoscale turbulence and dynamics at the global scale.

We have also shown evidence of the ergodic dynamics of wintertime near-surface submesoscale turbulence, meaning that temporally averaging flow properties is equivalent to averaging them spatially. For modeling and observational practices, this indicates that temporal and spatial resolutions are interdependent and should be considered together. The time interval used to archive data is as important as the spatial resolution. The submesoscale turbulence inferred from coarse temporal measurement resolution and high horizontal measurement resolution (6-hourly/$dx \sim 1$ km) is similar to that inferred from a combination of coarse horizontal and temporal measurement resolutions (6-hourly/$dx \sim 5$ km) or from coarse horizontal measurement resolution and high temporal measurement resolution (hourly/$dx \sim 10$ km).

For modeling, high temporal measurement resolution results in large storage or computational costs, whether offline or online strategies are used. Our results justify an online diagnostic to infer submesoscale turbulence from regional models or a parameterization strategy. For observational approaches, the high spatiotemporal resolution represents a challenge for measurement technologies. For example, the SWOT mission, which measures surface ocean topography on a global scale, combines relatively high horizontal resolution (2-km gridded product) with coarse temporal resolution (~20 day) (Morrow et al. 2019). Our findings emphasize the need to complement SWOT data with high spatiotemporal resolution in situ observations and model output in order to advance the dynamical interpretation of surface ocean observations.

Acknowledgments. P. T. and A. N.-G. acknowledge support from the Southern Ocean Carbon and Heat Impact on Climate (SO-CHIC) project, funded by the European Union's Horizon 2020 program under Grant Agreement 821001. P. T. and A. M. acknowledge funding from ONR Grant N00014-22-1-2082. A. M. also acknowledges funding from the NERC Grant NE/P018319/1. L. B. was supported by the Centre for Doctoral Training in Mathematics of Planet Earth, U.K. EPSRC funded (Grant EP/L016613/1). M. R. M. and S. T. G. acknowledge support from the NASA Surface Water and Ocean Topography (SWOT) Science Team (Award 80NSSC20K1136). M. R. M. and S. T. G. received additional support from NSF's Southern Ocean Carbon and Climate Observations and modelling (SOCCOM) Project under the NSF Award OPP-1936222, and S. T. G. was also supported by the NASA Ocean Surface Topography Science Team (Award 80NSSC21K1822). Computational resources provided by the Imperial College London Research Computing Service are gratefully acknowledged (https://doi.org/10.14469/hpc/2232). We want to thank Bruce Cornuelle for helpful discussions.

Data availability statement. Raw simulation data will be made available upon request to the authors. The *WOA18* and mixed layer depth climatologies and ARGO profiles are respectively available at https://www.ncei.noaa.gov/products/world-ocean-atlas, http://mixedlayer.ucsd.edu/, and https://www.seanoe.org/data/00412/52367/.

APPENDIX A

Lagrangian Filtering

a. *Performing the Lagrangian filtering*

Lagrangian filtering of the modeled oceanic fields in the Drake Passage was performed using the open source python package developed by Shakespeare et al. (2021). We filtered the three-dimensional hourly-averaged horizontal velocity for the whole period of the simulation considered in this work (30 days). The package makes use of the framework of OceanParcels (Delandmeter and Sebille 2019) to compute fluid parcel paths from velocities expressed in the Earth reference frame. Particles are initially seeded at each grid point. They are advected forward in time with a time step of 1 h over a time window of 1 day, and horizontal velocities are saved along the particles paths. This procedure is also done backward. The forward and backward trajectories are then combined to obtain the particles paths at a centered time and a resolution close to that of the model grid. This procedure allows to reduce sampling errors when interpolating variables back into the model grid in regions of large divergent flows (Shakespeare 2020; Jones et al. 2023). We used a filtering window of width ±1 day, following an approach that was previously used for our numerical simulation of the Drake Passage (Baker and Mashayek 2022) and which is based on the assessment of the filtered field sensitivity to the filtering window width presented by Shakespeare et al. (2021).

The Lagrangian filtering python package implements the following steps: 1) fluid parcel paths are assessed using standard Lagrangian tracking algorithm, 2) oceanic fields are interpolated to parcel paths, 3) fields are high-pass filtered

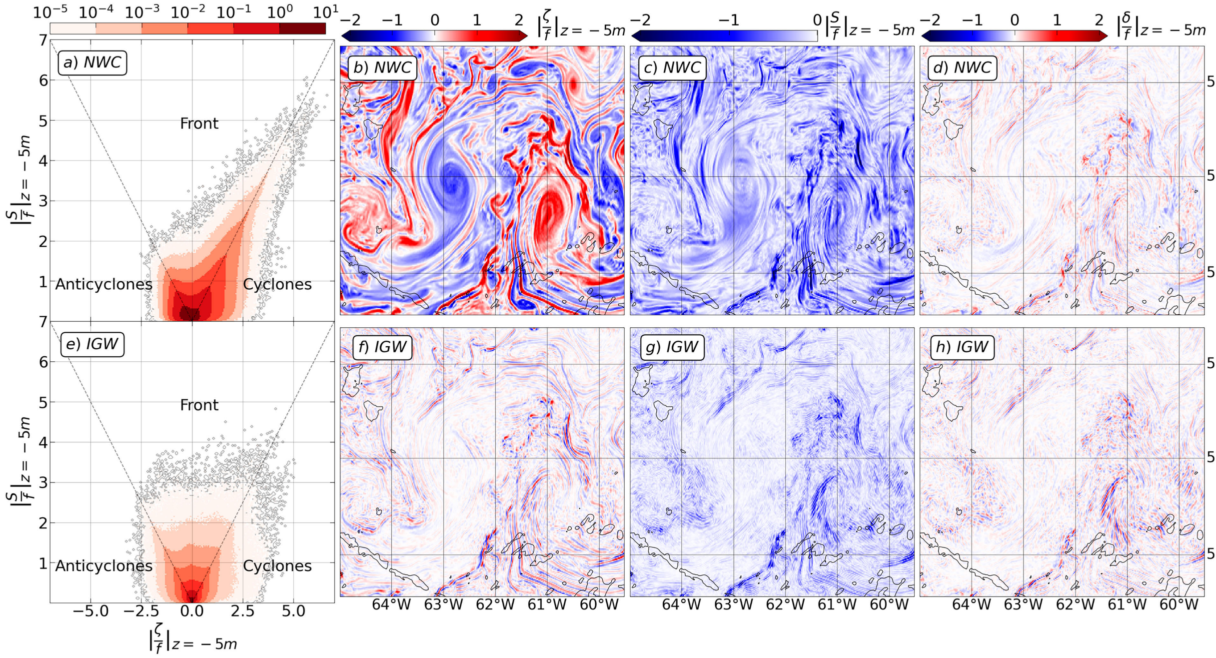

FIG. A1. Statistical characteristics of relative vorticity and strain for NWC and IGW motions. (a),(e) Vorticity–strain joint probability distribution functions inferred from 30-day time series of near-surface NWC horizontal velocities in (a) and IGW horizontal velocities in (e). Dotted black lines mark $|S/f| = \pm\zeta/f$. Note that the normalized strain corresponds to its absolute value. Horizontal sections of near-surface (b),(f) normalized relative vorticity (ζ/f), (c),(g) normalized strain (S/f), and (d),(h) normalized horizontal divergence (δ/f) for NWC motions in (b)–(d) and IGW motions in (f)–(h). Black contours show 1000- and 3000-m isobaths. Fields are plotted at a time step in the subregion shown in Fig. 2.

along parcel paths and saved at the time-centered parcel position, and 4) high-pass filtered fields are interpolated back to the model's grid. This procedure is repeated across depths and time. The high-pass filtered fields, in the frame of the flow, correspond to internal gravity waves (IGWs). The low-pass filtered fields correspond to nonwave currents (NWCs) and are obtained by subtracting the high-pass filtered fields (IGWs) from the total fields.

b. Evaluation of Lagrangian filtering for separating IGWs from NWCs

1) VORTICITY–STRAIN JOINT PROBABILITY DISTRIBUTION FUNCTIONS FOR NWC AND IGW MOTIONS

We evaluate the separation of the modeled velocity field into NWCs and IGWs, defined using the Lagrangian filtering approach [section 2b(1); Shakespeare et al. (2021)], using a statistical analysis of the velocity gradient tensor of the two classes of motions (Shcherbina et al. 2013; Rocha et al. 2016; Balwada et al. 2021). The two-dimensional velocity gradient tensor can be expressed in terms of the vertical component of relative vorticity [ζ in Eq. (A1)], horizontal divergence [δ in Eq. (A2)], and strain [S in Eq. (A3)]:

$$\zeta = \partial_x v - \partial_y u, \tag{A1}$$

$$\delta = \partial_x u + \partial_y v, \tag{A2}$$

$$S = \sqrt{(\partial_x u - \partial_y v)^2 + (\partial_x v + \partial_y u)^2}, \tag{A3}$$

with $\mathbf{u} = (u, v)$ representing the horizontal velocity components and $\nabla_H = (\partial_x, \partial_y)$ the horizontal component of the gradient operator.

Inspired by the statistical analysis used in Shcherbina et al. (2013), Rocha et al. (2016), Balwada et al. (2021), and Jones et al. (2023), we evaluate the characteristics of NWC motions using a joint probability distribution function of vorticity and strain. Submesoscale currents correspond to coherent features such as eddies, fronts, and filaments, which have distinct signatures on vorticity, strain, and divergence (Figs. A1b–d). Cyclonic eddies correspond to positive vorticity values, but weak strain; and fronts correspond to large vorticity, strain, and divergence values. Anticyclonic eddies are less intense than cyclonic eddies, and they correspond to negative vorticity of moderate magnitude. We extend the statistical analysis to IGW motions in order to evaluate the efficiency of the Lagrangian filtering at separating NWCs from IGWs. IGWs do not correspond to coherent two-dimensional features and are therefore not usually characterized using a vorticity–strain joint probability distribution function. However, a study showed that for near-surface turbulent regimes dominated by IGW motions, the vorticity–strain distributions correspond to weak values centered around the origin and distributed without characteristic shape (Rocha et al. 2016; Jones et al. 2023).

Figures A1a and A1e show vorticity–strain joint probability distribution functions computed from the 30-day time series of NWC and IGW near-surface velocities. Examples of near-surface relative vorticity, strain, and divergence,

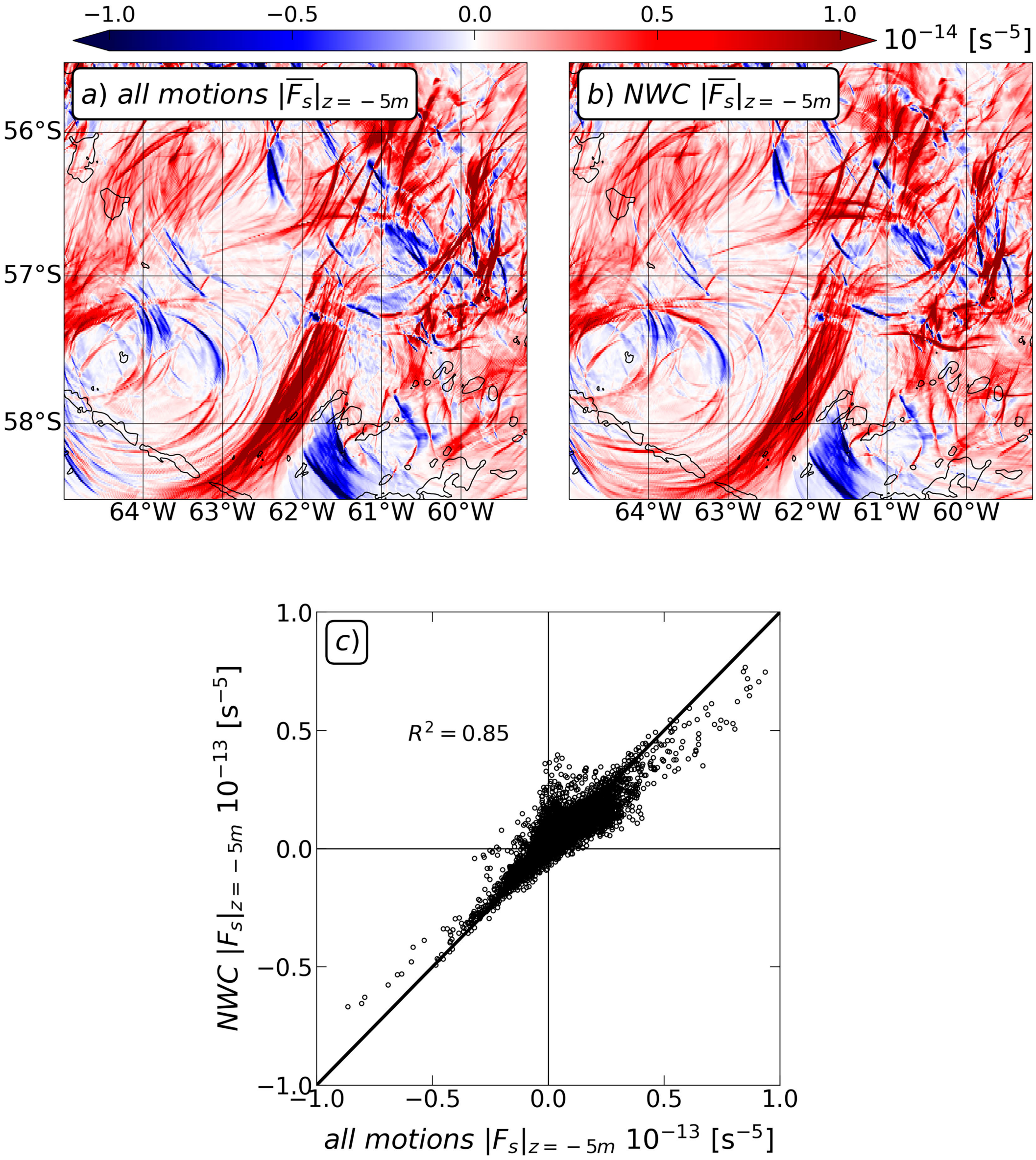

FIG. A2. Frontogenetic tendencies from all motions and NWC velocities. Horizontal sections of time-averaged (over 30-day simulation period) near-surface frontogenetic tendency [$\overline{F}_s = -(\partial_x \rho \nabla_H u + \partial_y \rho \nabla_H v) \cdot \nabla_H \rho$; (kg m^{-4})^2 s^{-1}; with (u, v) the horizontal velocities and ρ the density] inferred from (a) all motions and (b) NWC horizontal velocities. Black contours show 1000- and 3000-m isobaths. Fields are plotted in the subregion shown in Fig. 2. (c) Scatter distribution of (a) plotted as a function of (b), with R^2 the linear correlation coefficient.

normalized by the Coriolis parameter, for NWC and IGW motions are also shown at a time step (Figs. A1b–d,f–g). The vorticity–strain distribution for NWC motions has the characteristic shape of submesoscale currents (Fig. A1a), which has been documented in different regions from observations and models (Shcherbina et al. 2013; Rocha et al. 2016; Balwada et al. 2021). The vorticity–strain distribution is centered around the origin and extends along the lines of $|S| = \pm\zeta$, with a strong positive skewness. This shape depicts fronts, which are characterized by strain of equal or larger values than vorticity (Figs. A1b,c). The structural difference between positive and negative vorticity (positive skewness) indicates that cyclonic fronts and eddies are more intense (Figs. A1b,c). This comes from intense anticyclonic vorticity being unstable at submesoscale, which is not the case of cyclonic vorticity (Hoskins and Bretherton 1972; Shcherbina et al. 2013).

The vorticity–strain distribution for IGW motions has a squared shape, in contrast with NWC motions (Fig. A1e). The vorticity–strain distribution is centered around the origin and extends to values of uniform moderate magnitudes in all directions without showing distinct extrema. This is consistent with

IGW not accounting for coherent two-dimensional features and corresponding to background wave trains of vorticity, strain, and divergence patterns (Figs. A1f–h).

In summary, vorticity–strain joint probability distribution functions for NWC and IGW motions have distinct shapes, consistent with the typical characteristics of near-surface turbulent regimes dominated by submesoscale currents and internal gravity waves, respectively, which have been documented in other oceanic regions (Shcherbina et al. 2013; Rocha et al. 2016; Balwada et al. 2021). It indicates that 1) NWC and IGW classes of motions respectively account for the bulk of submesoscale currents and internal gravity waves, and subsequently that 2) the Lagrangian filtering is a robust approach at separating the two classes of motions in the context of our regional numerical simulation of the Drake Passage in winter.

2) FRONTOGENETIC TENDENCY FOR TOTAL AND NWC MOTIONS

We further our evaluation of the separation of the modeled velocity field into NWCs and IGWs [section 2b(1)] by comparing the frontogenetic tendency inferred from total and NWC velocities. The frontogenetic tendency $[F_s = -(\partial_x \rho \nabla_H u + \partial_y \rho \nabla_H v) \cdot \nabla_H \rho]$ measures the rate of intensification of buoyancy gradients at fronts, and frontogenesis (positive values) should be associated with submesoscale fronts (Hoskins 1982).

Figure A2 shows the time-averaged frontogenetic tendency computed from total and NWC near-surface velocities, and their correlation in the all motions $\overline{F_s}$–NWC $\overline{F_s}$ space. NWC motions are the main contributor to the total frontogenetic tendency, confirming that NWCs account for the bulk of submesoscale fronts. Both forms of frontogenetic tendency show highly similar patterns and magnitudes (Figs. A2a,b) and are highly correlated (Fig. A2c). The two tendencies differ slightly from their magnitudes. The total tendency has slightly higher positive magnitudes than the NWC one, as shown from the moderate density of positive values below the identity curve in the all motions $\overline{F_s}$–NWC $\overline{F_s}$ space. The magnitude difference points toward the contribution of IGWs in intensifying fronts. This indicates that IGWs weakly enhance submesoscale fronts, as documented from in situ observations and idealized numerical simulations (Alford et al. 2013; Vanneste 2013; Nagai et al. 2015; Shakespeare and Hogg 2017).

The good agreement between the total and NWC frontogenetic tendencies indicates that 1) NWC motions do the bulk of frontogenesis and 2) are therefore primarily associated with eddies and submesoscale fronts, confirming the robustness of the Lagrangian filtering approach in the context of our numerical simulation. Note that vorticity, strain, and frontogenetic tendency are used to evaluate the separation of NWC from IGW (Figs. A1 and A2), but it would not be suitable to base a separation method upon these variables. Indeed, NWC and IGW motions differ from their probability density functions of vorticity–strain and frontogenetic tendencies (Figs. A1a,e and A2c), but not from the magnitude and sign of raw vorticity, strain, and frontogenetic tendencies (Figs. A1b–d,f–h and A2a,b), making separation methods based on values of these variables inadequate. Another issue with any separation methods in the Earth reference frame is that they do not bypass the Doppler shifting, which modulate the propagation of IGW and therefore do not allow to accurately isolate IGW and NWC in the Earth reference frame (Shakespeare et al. 2021).

APPENDIX B

The Computation of Helmholtz Decomposition

The Helmholtz decomposition of the modeled flows in the Drake Passage was performed by solving a Poisson equation for the divergence of the horizontal velocities using Dirichlet boundary conditions (Gula et al. 2014; Srinivasan et al. 2023). We decomposed the three-dimensional NWC and IGW horizontal velocities for the whole period of the simulation (30 days).

Before the Helmholtz decomposition is performed, horizontal velocity fields are interpolated on a regular Cartesian grid. The Poisson equation is solved for the divergence of the two-dimensional horizontal velocities, at one depth and at a time step. This procedure is repeated across depths and time. Rotational (nondivergent) velocities are obtained by subtracting divergent velocities from the total velocities.

APPENDIX C

The Computation of Cross-Scale Kinetic Energy Flux

Cross-scale KE flux were computed at the near surface (0–100-m depth) using the coarse-graining approach with respect to spatial scales (Aluie et al. 2018; Schubert et al. 2020; Srinivasan et al. 2023). The procedure to compute cross-scale KE flux is the following: 1) two-dimensional (x, y) horizontal components of velocity [$u(x, y)$, $v(x, y)$] are interpolated on a regular Cartesian grid, 2) velocities and quadratic velocities (u^2, v^2, uv) are low- and high-pass spatially filtered, for a given cutoff spatial scales, using a top-hat kernel, and 3) cross-scale KE flux are computed by combining the different filtered variables. The procedure is repeated over depths, time, and different cutoff spatial scale (l = 1, 2, 3, 4, 5, 10, 15, 20, 25, 30, 40, 50, 75, and 100 km).

The coarse-graining method is a local approach that allows us to estimate cross-scale KE flux in the physical space. This approach was preferred relative to the spectral approach, because it relies on fewer approximations (no approximations of isotropic and homogeneous turbulence). The KE spectra (Figs. 5 and 6a) and cross-scale KE flux (Figs. 6b–d, 7c, and 8) presented in this study are interpreted jointly knowing that the cutoff spatial scale, used for the coarse-grained method, corresponds to half the wavelength for the spectral analysis.

APPENDIX D

The Computation of Kinetic Energy Spectra

Spectral analyses were performed in two-dimensional frequency (ω in the Earth reference frame) and wavenumber

(K) spaces and one-dimensional wavenumber (K) space, in a subdomain of the Drake Passage (large enough to resolve wavelengths in the range 2–150 km) and for the whole period of the simulation (long enough to resolve frequencies in the range from 2 h to 25 days). Horizontal velocities are preprocessed before computing KE spectra. Velocities are interpolated onto a regular Cartesian grid. The mean and linear trends in time (t) and horizontal space (x, y) are removed from the three-dimensional velocities (t, x, y), which are then multiplied by a three-dimensional Hanning window conserving energy density.

The procedure to compute frequency–wavenumber KE spectra is the following: 1) a discrete three-dimensional Fourier transform (ω, k, l; with k, l the zonal and meridional wavenumbers) is computed for the two components of preprocessed horizontal velocities, 2) Fourier transforms are converted into power spectral densities and azimuthally averaged over k and l, to transform three-dimensional spectral densities into two-dimensional spectral densities (ω, K; with K the isotropic wavenumber), and 3) frequency–wavenumber spectra for kinetic energy are then obtained by combining spectra of the horizontal velocities.

The procedure to compute horizontal wavenumber KE spectra is similar to the procedure for frequency–wavenumber KE spectra. The computed Fourier transform is two-dimensional (k, l) and the procedure is repeated across time. The time-averaged wavenumber KE spectra are obtained by averaging the spectra for each time step.

REFERENCES

Ajayi, A., J. L. Sommer, E. P. Chassignet, J.-M. Molines, X. Xu, A. Albert, and W. Dewar, 2021: Diagnosing cross-scale kinetic energy exchanges from two submesoscale permitting ocean models. *J. Adv. Model. Earth Syst.*, **13**, e2019MS001923, https://doi.org/10.1029/2019MS001923.

Alford, M. H., A. Y. Shcherbina, and M. C. Gregg, 2013: Observations of near-inertial internal gravity waves radiating from a frontal jet. *J. Phys. Oceanogr.*, **43**, 1225–1239, https://doi.org/10.1175/JPO-D-12-0146.1.

——, J. A. MacKinnon, H. L. Simmons, and J. D. Nash, 2016: Near-inertial internal gravity waves in the ocean. *Annu. Rev. Mar. Sci.*, **8**, 95–123, https://doi.org/10.1146/annurev-marine-010814-015746.

Aluie, H., M. Hecht, and G. K. Vallis, 2018: Mapping the energy cascade in the North Atlantic Ocean: The coarse-graining approach. *J. Phys. Oceanogr.*, **48**, 225–244, https://doi.org/10.1175/JPO-D-17-0100.1.

Arbic, B. K., and Coauthors, 2022: Near-surface oceanic kinetic energy distributions from drifter observations and numerical models. *J. Geophys. Res. Oceans*, e2022JC018551, https://doi.org/10.1029/2022JC018551.

Bachman, S. D., J. A. Kleypas, M. Erdmann, and E. Setyawan, 2022: A global atlas of potential thermal refugia for coral reefs generated by internal gravity waves. *Front. Mar. Sci.*, **9**, 921879, https://doi.org/10.3389/fmars.2022.921879.

Baker, L. E., and A. Mashayek, 2021: Surface reflection of bottom generated oceanic lee waves. *J. Fluid Mech.*, **924**, A17, https://doi.org/10.1017/jfm.2021.627.

——, and ——, 2022: The impact of representations of realistic topography on parameterized oceanic lee wave energy flux. *J. Geophys. Res. Oceans*, **127**, e2022JC018995, https://doi.org/10.1029/2022JC018995.

——, ——, and A. C. N. Garabato, 2023: Boundary upwelling of Antarctic bottom water by topographic turbulence. *AGU Adv.*, **4**, e2022AV000858, https://doi.org/10.1029/2022AV000858.

Balwada, D., Q. Xiao, S. Smith, R. Abernathey, and A. Gray, 2021: Vertical fluxes conditioned on vorticity and strain reveal submesoscale ventilation. *J. Phys. Oceanogr.*, **51**, 2883–2901, https://doi.org/10.1175/JPO-D-21-0016.1.

Barkan, R., K. B. Winters, and J. C. McWilliams, 2017: Stimulated imbalance and the enhancement of eddy kinetic energy dissipation by internal waves. *J. Phys. Oceanogr.*, **47**, 181–198, https://doi.org/10.1175/JPO-D-16-0117.1.

——, K. Srinivasan, L. Yang, J. C. McWilliams, J. Gula, and C. Vic, 2021: Oceanic mesoscale eddy depletion catalyzed by internal waves. *Geophys. Res. Lett.*, **48**, e2021GL094376, https://doi.org/10.1029/2021GL094376.

Bartello, P., 1995: Geostrophic adjustment and inverse cascades in rotating stratified turbulence. *J. Atmos. Sci.*, **52**, 4410–4428, https://doi.org/10.1175/1520-0469(1995)052<4410:GAAICI>2.0.CO;2.

Boccaletti, G., R. Ferrari, and B. Fox-Kemper, 2007: Mixed layer instabilities and restratification. *J. Phys. Oceanogr.*, **37**, 2228–2250, https://doi.org/10.1175/JPO3101.1.

Boyd, J. P., 1992: The energy spectrum of fronts: Time evolution of shocks in Burgers equation. *J. Atmos. Sci.*, **49**, 128–139, https://doi.org/10.1175/1520-0469(1992)049<0128:TESOFT>2.0.CO;2.

Bretherton, F. P., and C. J. R. Garrett, 1968: Wavetrains in inhomogeneous moving media. *Proc. Roy. Soc. London*, **302A**, 529–554, https://doi.org/10.1098/rspa.1968.0034.

Bühler, O., J. Callies, and R. Ferrari, 2014: Wave–vortex decomposition of one-dimensional ship-track data. *J. Fluid Mech.*, **756**, 1007–1026, https://doi.org/10.1017/jfm.2014.488.

Callies, J., and R. Ferrari, 2013: Interpreting energy and tracer spectra of upper-ocean turbulence in the submesoscale range (1–200 km). *J. Phys. Oceanogr.*, **43**, 2456–2474, https://doi.org/10.1175/JPO-D-13-063.1.

Capet, X., J. C. McWilliams, M. J. Molemaker, and A. F. Shchepetkin, 2008a: Mesoscale to submesoscale transition in the California Current System. Part II: Frontal processes. *J. Phys. Oceanogr.*, **38**, 44–64, https://doi.org/10.1175/2007JPO3672.1.

——, ——, ——, and ——, 2008b: Mesoscale to submesoscale transition in the California Current System. Part III: Energy balance and flux. *J. Phys. Oceanogr.*, **38**, 2256–2269, https://doi.org/10.1175/2008JPO3810.1.

Capó, E., and J. C. McWilliams, 2022: Coherent Lagrangian pathways near an East Alboran Front. *J. Geophys. Res. Oceans*, **127**, e2021JC018022, https://doi.org/10.1029/2021JC018022.

Charney, J. G., 1971: Geostrophic turbulence. *J. Atmos. Sci.*, **28**, 1087–1095, https://doi.org/10.1175/1520-0469(1971)028<1087:GT>2.0.CO;2.

Chelton, D. B., M. G. Schlax, and R. M. Samelson, 2011: Global observations of nonlinear mesoscale eddies. *Prog. Oceanogr.*, **91**, 167–216, https://doi.org/10.1016/j.pocean.2011.01.002.

Chen, Y., S. Speich, and R. Laxenaire, 2022: Formation and transport of the South Atlantic subtropical mode water in eddy-permitting observations. *J. Geophys. Res. Oceans*, **127**, e2021JC017767, https://doi.org/10.1029/2021JC017767.

Cusack, J. M., J. A. Brearley, A. C. Naveira Garabato, D. A. Smeed, K. L. Polzin, N. Velzeboer, and C. J. Shakespeare, 2020: Observed eddy–internal wave interactions in the Southern Ocean. *J. Phys. Oceanogr.*, **50**, 3043–3062, https://doi.org/10.1175/JPO-D-20-0001.1.

Cutolo, E., and Coauthors, 2022: Diagnosing frontal dynamics from observations using a variational approach. *J. Geophys. Res. Oceans*, **127**, e2021JC018336, https://doi.org/10.1029/2021JC018336.

Delandmeter, P., and E. V. Sebille, 2019: The Parcels v2.0 Lagrangian framework: New field interpolation schemes. *Geosci. Model Dev.*, **12**, 3571–3584, https://doi.org/10.5194/gmd-12-3571-2019.

De Marez, C., N. Lahaye, and J. Gula, 2020: Interaction of the Gulf Stream with small scale topography: A focus on lee waves. *Sci. Rep.*, **10**, 2332, https://doi.org/10.1038/s41598-020-59297-5.

Dong, J., B. Fox-Kemper, H. Zhang, and C. Dong, 2020: The seasonality of submesoscale energy production, content, and cascade. *Geophys. Res. Lett.*, **47**, e2020GL087388, https://doi.org/10.1029/2020GL087388.

Dong, S., J. Sprintall, S. T. Gille, and L. Talley, 2008: Southern Ocean mixed-layer depth from Argo float profiles. *J. Geophys. Res.*, **113**, C06013, https://doi.org/10.1029/2006JC004051.

Dunphy, M., and K. G. Lamb, 2014: Focusing and vertical mode scattering of the first mode internal tide by mesoscale eddy interaction. *J. Geophys. Res. Oceans*, **119**, 523–536, https://doi.org/10.1002/2013JC009293.

Ferrari, R., and C. Wunsch, 2009: Ocean circulation kinetic energy: Reservoirs, sources, and sinks. *Annu. Rev. Fluid Mech.*, **41**, 253–282, https://doi.org/10.1146/annurev.fluid.40.111406.102139.

——, and ——, 2010: The distribution of eddy kinetic and potential energies in the global ocean. *Tellus*, **62A**, 92–108, https://doi.org/10.3402/tellusa.v62i2.15680.

Fox-Kemper, B., R. Ferrari, and R. Hallberg, 2008: Parameterization of mixed layer eddies. Part I: Theory and diagnosis. *J. Phys. Oceanogr.*, **38**, 1145–1165, https://doi.org/10.1175/2007JPO3792.1.

——, L. Johnson, and F. Qiao, 2022: Ocean near-surface layers. *Ocean Mixing*, Elsevier, 65–94.

Freilich, M., L. Lenain, and S. T. Gille, 2023: Characterizing the role of non-linear interactions in the transition to submesoscale dynamics at a dense filament. *Geophys. Res. Lett.*, **50**, e2023GL103745, https://doi.org/10.1029/2023GL103745.

Garrett, C., and W. Munk, 1972: Space-time scales of internal waves. *Geophys. Fluid Dyn.*, **3**, 225–264, https://doi.org/10.1080/03091927208236082.

Gill, A. E., 1982: *Atmosphere–Ocean Dynamics*. International Geophysics Series, Vol. 30, Academic Press, 662 pp.

Griffies, S., and Coauthors, 2015: Impacts on ocean heat from transient mesoscale eddies in a hierarchy of climate models. *J. Climate*, **28**, 952–977, https://doi.org/10.1175/JCLI-D-14-00353.1.

Gula, J., M. Molemaker, and J. McWilliams, 2014: Submesoscale cold filaments in the Gulf Stream. *J. Phys. Oceanogr.*, **44**, 2617–2643, https://doi.org/10.1175/JPO-D-14-0029.1.

——, J. Taylor, A. Shcherbina, and A. Mahadevan, 2022: Submesoscale processes and mixing. *Ocean Mixing: Drivers, Mechanisms and Impacts*, M. Meredith and A. Naveira Garabato, Eds., Elsevier, 181–214, https://doi.org/10.1016/B978-0-12-821512-8.00015-3.

Haine, T. W. N., and J. Marshall, 1998: Gravitational, symmetric, and baroclinic instability of the ocean mixed layer. *J. Phys. Oceanogr.*, **28**, 634–658, https://doi.org/10.1175/1520-0485(1998)028<0634:GSABIO>2.0.CO;2.

Hallberg, R., and A. Gnanadesikan, 2006: The role of eddies in determining the structure and response of the wind-driven Southern Hemisphere overturning: Results from the Modeling Eddies in the Southern Ocean (MESO) project. *J. Phys. Oceanogr.*, **36**, 2232–2252, https://doi.org/10.1175/JPO2980.1.

Holte, J., L. Talley, J. Gilson, and D. Roemmich, 2017: An Argo mixed layer climatology and database. *Geophys. Res. Lett.*, **44**, 5618–5626, https://doi.org/10.1002/2017GL073426.

Hoskins, B. J., 1982: The mathematical theory of frontogenesis. *Annu. Rev. Fluid Mech.*, **14**, 131–151, https://doi.org/10.1146/annurev.fl.14.010182.001023.

——, and F. Bretherton, 1972: Atmospheric frontogenesis models: Mathematical formulation and solution. *J. Atmos. Sci.*, **29**, 11–37, https://doi.org/10.1175/1520-0469(1972)029<0011:AFMMFA>2.0.CO;2.

Hughes, C., and C. Wilson, 2008: Wind work on the geostrophic ocean circulation: An observational study of the effect of small scales in the wind stress. *J. Geophys. Res.*, **113**, C02016, https://doi.org/10.1029/2007JC004371.

Jones, C., Q. Xiao, R. Abernathey, and K. Smith, 2023: Using Lagrangian filtering to remove waves from the ocean surface velocity field. *J. Adv. Model. Earth Syst.*, **15**, e2022MS003220, https://doi.org/10.1029/2022MS003220.

Klein, P., and Coauthors, 2019: Ocean-scale interactions from space. *Earth Space Sci.*, **6**, 795–817, https://doi.org/10.1029/2018EA000492.

Kolodziejczyk, N., A. Prigent-Mazella, and F. Gaillard, 2021: ISAS temperature and salinity gridded fields. SEANOE, accessed 4 October 2023, https://doi.org/10.17882/52367.

Kunze, E., 1985: Near-inertial wave propagation in geostrophic shear. *J. Phys. Oceanogr.*, **15**, 544–565, https://doi.org/10.1175/1520-0485(1985)015<0544:NIWPIG>2.0.CO;2.

Lahaye, N., J. Gula, and G. Roullet, 2019: Sea surface signature of internal tides. *Geophys. Res. Lett.*, **46**, 3880–3890, https://doi.org/10.1029/2018GL081848.

Large, W., J. McWilliams, and S. Doney, 1994: Oceanic vertical mixing: A review and a model with a nonlocal boundary layer parameterization. *Rev. Geophys.*, **32**, 363–403, https://doi.org/10.1029/94RG01872.

Le Boyer, A., and M. Alford, 2021: Variability and sources of the internal wave continuum examined from global moored velocity records. *J. Phys. Oceanogr.*, **51**, 2807–2823, https://doi.org/10.1175/JPO-D-20-0155.1.

Locarnini, M., and Coauthors, 2018: *Temperature*. Vol. 1, *World Ocean Atlas 2018*, NOAA Atlas NESDIS 81, 52 pp., https://data.nodc.noaa.gov/woa/WOA18/DOC/woa18_vol1.pdf.

Marshall, J., A. Adcroft, C. Hill, L. Perelman, and C. Heisey, 1997: A finite-volume, incompressible Navier Stokes model for studies of the ocean on parallel computers. *J. Geophys. Res.*, **102**, 5753–5766, https://doi.org/10.1029/96JC02775.

Mashayek, A., R. Ferrari, S. Merrifield, J. R. Ledwell, L. S. Laurent, and A. Naveira Garabato, 2017: Topographic enhancement of vertical turbulent mixing in the Southern Ocean. *Nat. Commun.*, **8**, 14197, https://doi.org/10.1038/ncomms14197.

McWilliams, J. C., 2016: Submesoscale currents in the ocean. *Proc. Roy. Soc.*, **472A**, 20160117, https://doi.org/10.1098/rspa.2016.0117.

——, 2021: Oceanic frontogenesis. *Annu. Rev. Mar. Sci.*, **13**, 227–253, https://doi.org/10.1146/annurev-marine-032320-120725.

Molemaker, M., J. McWilliams, and X. Capet, 2010: Balanced and unbalanced routes to dissipation in an equilibrated Eady flow. *J. Fluid Mech.*, **654**, 35–63, https://doi.org/10.1017/S0022112009993272.

Morrow, R., and Coauthors, 2019: Global observations of fine-scale ocean surface topography with the Surface Water and Ocean Topography (SWOT) mission. *Front. Mar. Sci.*, **6**, 232, https://doi.org/10.3389/fmars.2019.00232.

Müller, P., J. McWilliams, and M. Molemaker, 2005: Routes to dissipation in the ocean: The 2D/3D turbulence conundrum. *Marine Turbulence: Theories, Observations and Models*, Cambridge University Press, 397–405.

Munk, W., 1981: Internal waves and small-scale processes. *Evolution of Physical Oceanography: Scientific Surveys in Honor of Henry Stommel*, MIT Press, 264–291.

Nagai, T., A. Tandon, E. Kunze, and A. Mahadevan, 2015: Spontaneous generation of near-inertial waves by the Kuroshio Front. *J. Phys. Oceanogr.*, **45**, 2381–2406, https://doi.org/10.1175/JPO-D-14-0086.1.

Naveira Garabato, A. C., X. Yu, J. Callies, R. Barkan, K. L. Polzin, E. E. Frajka-Williams, C. E. Buckingham, and S. M. Griffies, 2022: Kinetic energy transfers between mesoscale and submesoscale motions in the open ocean's upper layers. *J. Phys. Oceanogr.*, **52**, 75–97, https://doi.org/10.1175/JPO-D-21-0099.1.

Nikurashin, M., and R. Ferrari, 2011: Global energy conversion rate from geostrophic flows into internal lee waves in the deep ocean. *Geophys. Res. Lett.*, **38**, L08610, https://doi.org/10.1029/2011GL046576.

Olbers, D., 1976: Nonlinear energy transfer and the energy balance of the internal wave field in the deep ocean. *J. Fluid Mech.*, **74**, 375–399, https://doi.org/10.1017/S0022112076001857.

——, F. Pollmann, and C. Eden, 2020: On psi interactions in internal gravity wave fields and the decay of baroclinic tides. *J. Phys. Oceanogr.*, **50**, 751–771, https://doi.org/10.1175/JPO-D-19-0224.1.

Polzin, K., 2010: Mesoscale eddy–internal wave coupling. Part II: Energetics and results from PolyMode. *J. Phys. Oceanogr.*, **40**, 789–801, https://doi.org/10.1175/2009JPO4039.1.

——, and Y. Lvov, 2011: Toward regional characterizations of the oceanic internal wavefield. *Rev. Geophys.*, **49**, RG4003, https://doi.org/10.1029/2010RG000329.

Qiu, B., S. Chen, P. Klein, H. Sasaki, and Y. Sasai, 2014: Seasonal mesoscale and submesoscale eddy variability along the North Pacific Subtropical Countercurrent. *J. Phys. Oceanogr.*, **44**, 3079–3098, https://doi.org/10.1175/JPO-D-14-0071.1.

——, ——, ——, J. Wang, H. Torres, L.-L. Fu, and D. Menemenlis, 2018: Seasonality in transition scale from balanced to unbalanced motions in the world ocean. *J. Phys. Oceanogr.*, **48**, 591–605, https://doi.org/10.1175/JPO-D-17-0169.1.

Rama, J., C. J. Shakespeare, and A. M. Hogg, 2022a: Importance of background vorticity effect and Doppler shift in defining near-inertial internal waves. *Geophys. Res. Lett.*, **49**, e2022GL099498, https://doi.org/10.1029/2022GL099498.

——, C. Shakespeare, and A. Hogg, 2022b: The wavelength dependence of the propagation of near-inertial internal waves. *J. Phys. Oceanogr.*, **52**, 2493–2514, https://doi.org/10.1175/JPO-D-21-0266.1.

Rhines, P., 1977: The dynamics of unsteady currents. *Marine Modeling*, E. D. Goldberg et al., Eds., *The Sea—Ideas and Observations on Progress in the Study of the Seas*, Vol. 6, John Wiley and Sons, 189–318.

——, 1979: Geostrophic turbulence. *Annu. Rev. Fluid Mech.*, **11**, 401–441, https://doi.org/10.1146/annurev.fl.11.010179.002153.

Rocha, C., S. Gille, T. Chereskin, and D. Menemenlis, 2016: Seasonality of submesoscale dynamics in the Kuroshio Extension. *Geophys. Res. Lett.*, **43**, 11 304–11 311, https://doi.org/10.1002/2016GL071349.

——, G. Wagner, and W. Young, 2018: Stimulated generation: Extraction of energy from balanced flow by near-inertial waves. *J. Fluid Mech.*, **847**, 417–451, https://doi.org/10.1017/jfm.2018.308.

Salmon, R., 1980: Baroclinic instability and geostrophic turbulence. *Geophys. Astrophys. Fluid Dyn.*, **15**, 167–211, https://doi.org/10.1080/03091928008241178.

Sasaki, H., P. Klein, B. Qiu, and Y. Sasai, 2014: Impact of oceanic-scale interactions on the seasonal modulation of ocean dynamics by the atmosphere. *Nat. Commun.*, **5**, 5636, https://doi.org/10.1038/ncomms6636.

——, ——, Y. Sasai, and B. Qiu, 2017: Regionality and seasonality of submesoscale and mesoscale turbulence in the North Pacific Ocean. *Ocean Dyn.*, **67**, 1195–1216, https://doi.org/10.1007/s10236-017-1083-y.

Savage, A., and Coauthors, 2017: Spectral decomposition of internal gravity wave sea surface height in global models. *J. Geophys. Res. Oceans*, **122**, 7803–7821, https://doi.org/10.1002/2017JC013009.

Schubert, R., F. Schwarzkopf, B. Baschek, and A. Biastoch, 2019: Submesoscale impacts on mesoscale Agulhas dynamics. *J. Adv. Model. Earth Syst.*, **11**, 2745–2767, https://doi.org/10.1029/2019MS001724.

——, J. Gula, R. Greatbatch, B. Baschek, and A. Biastoch, 2020: The submesoscale kinetic energy cascade: Mesoscale absorption of submesoscale mixed layer eddies and frontal downscale fluxes. *J. Phys. Oceanogr.*, **50**, 2573–2589, https://doi.org/10.1175/JPO-D-19-0311.1.

Shakespeare, C., 2020: Interdependence of internal tide and lee wave generation at abyssal hills: Global calculations. *J. Phys. Oceanogr.*, **50**, 655–677, https://doi.org/10.1175/JPO-D-19-0179.1.

——, and A. Hogg, 2017: Spontaneous surface generation and interior amplification of internal waves in a regional-scale ocean model. *J. Phys. Oceanogr.*, **47**, 811–826, https://doi.org/10.1175/JPO-D-16-0188.1.

——, A. Gibson, A. Hogg, S. Bachman, S. Keating, and N. Velzeboer, 2021: A new open source implementation of Lagrangian filtering: A method to identify internal waves in high-resolution simulations. *J. Adv. Model. Earth Syst.*, **13**, e2021MS002616, https://doi.org/10.1029/2021MS002616.

Shcherbina, A., E. D'Asaro, C. Lee, J. Klymak, M. Molemaker, and J. McWilliams, 2013: Statistics of vertical vorticity, divergence, and strain in a developed submesoscale turbulence field. *Geophys. Res. Lett.*, **40**, 4706–4711, https://doi.org/10.1002/grl.50919.

Simmons, A., S. Uppala, D. Dee, and S. Kobayashi, 2006: ERA-Interim: New ECMWF reanalysis products from 1989 onwards. *ECMWF Newsletter*, No. 110, ECMWF, Reading, United Kingdom, 25–36, https://www.ecmwf.int/sites/default/files/elibrary/2006/14615-newsletter-no110-winter-200607.pdf.

Skamarock, W. C., 2004: Evaluating mesoscale NWP models using kinetic energy spectra. *Mon. Wea. Rev.*, **132**, 3019–3032, https://doi.org/10.1175/MWR2830.1.

Song, H., J. Marshall, J.-M. Campin, and J. D. J. McGillicuddy, 2019: Impact of near-inertial waves on vertical mixing and air-sea CO_2 fluxes in the Southern Ocean. *J. Geophys. Res. Oceans*, **124**, 4605–4617, https://doi.org/10.1029/2018JC014928.

Soufflet, Y., P. Marchesiello, F. Lemarié, J. Jouanno, X. Capet, L. Debreu, and R. Benshila, 2016: On effective resolution in ocean models. *Ocean Modell.*, **98**, 36–50, https://doi.org/10.1016/j.ocemod.2015.12.004.

Srinivasan, K., R. Barkan, and J. McWilliams, 2023: A forward energy flux at submesoscales driven by frontogenesis. *J. Phys. Oceanogr.*, **53**, 287–305, https://doi.org/10.1175/JPO-D-22-0001.1.

Stone, P., 1970: On non-geostrophic baroclinic stability: Part II. *J. Atmos. Sci.*, **27**, 721–726, https://doi.org/10.1175/1520-0469(1970)027<0721:ONGBSP>2.0.CO;2.

Sugiyama, Y., Y. Niwa, and T. Hibiya, 2009: Numerically reproduced internal wave spectra in the deep ocean. *Geophys. Res. Lett.*, **36**, L07601, https://doi.org/10.1029/2008GL036825.

Sun, B., C. Liu, and F. Wang, 2019: Global meridional eddy heat transport inferred from Argo and altimetry observations. *Sci. Rep.*, **9**, 1345, https://doi.org/10.1038/s41598-018-38069-2.

Tamsitt, V., and Coauthors, 2017: Spiraling pathways of global deep waters to the surface of the Southern Ocean. *Nat. Commun.*, **8**, 172, https://doi.org/10.1038/s41467-017-00197-0.

Taylor, J., and A. Thompson, 2022: Submesoscale dynamics in the upper ocean. *Annu. Rev. Fluid Mech.*, **55**, 103–127, https://doi.org/10.1146/annurev-fluid-031422-095147.

Thomas, J., and S. Arun, 2020: Near-inertial waves and geostrophic turbulence. *Phys. Rev. Fluids*, **5**, 014801, https://doi.org/10.1103/PhysRevFluids.5.014801.

——, and D. Daniel, 2021: Forward flux and enhanced dissipation of geostrophic balanced energy. *J. Fluid Mech.*, **911**, A60, https://doi.org/10.1017/jfm.2020.1026.

Thompson, A. F., and A. C. Naveira Garabato, 2014: Equilibration of the Antarctic Circumpolar Current by standing meanders. *J. Phys. Oceanogr.*, **44**, 1811–1828, https://doi.org/10.1175/JPO-D-13-0163.1.

Torres, H., P. Klein, D. Menemenlis, B. Qiu, Z. Su, J. Wang, S. Chen, and L.-L. Fu, 2018: Partitioning ocean motions into balanced motions and internal gravity waves: A modeling study in anticipation of future space missions. *J. Geophys. Res. Oceans*, **123**, 8084–8105, https://doi.org/10.1029/2018JC014438.

——, and Coauthors, 2022: Separating energetic internal gravity waves and small-scale frontal dynamics. *Geophys. Res. Lett.*, **49**, e2021GL096249, https://doi.org/10.1029/2021GL096249.

Tulloch, R., and Coauthors, 2014: Direct estimate of lateral eddy diffusivity upstream of Drake Passage. *J. Phys. Oceanogr.*, **44**, 2593–2616, https://doi.org/10.1175/JPO-D-13-0120.1.

Uchida, T., R. Abernathey, and S. Smith, 2017: Seasonality of eddy kinetic energy in an eddy permitting global climate model. *Ocean Modell.*, **118**, 41–58, https://doi.org/10.1016/j.ocemod.2017.08.006.

Vanneste, J., 2013: Balance and spontaneous wave generation in geophysical flows. *Annu. Rev. Fluid Mech.*, **45**, 147–172, https://doi.org/10.1146/annurev-fluid-011212-140730.

Whitt, D., and L. Thomas, 2015: Resonant generation and energetics of wind-forced near-inertial motions in a geostrophic flow. *J. Phys. Oceanogr.*, **45**, 181–208, https://doi.org/10.1175/JPO-D-14-0168.1.

Wunsch, C., 2007: The past and future ocean circulation from a contemporary perspective. *Ocean Circulation: Mechanisms and Impacts—Past and Future Changes of Meridional Overturning*, *Geophys. Monogr.*, Vol. 173, Amer. Geophys. Union, 53–74, https://doi.org/10.1029/173GM06.

Zweng, M., and Coauthors, 2019: *Salinity*. Vol. 2, *World Ocean Atlas 2018*, NOAA Atlas NESDIS 82, 50 pp., https://data.nodc.noaa.gov/woa/WOA18/DOC/woa18_vol2.pdf.